Identification of Influence Lines for Highway Bridges Using Bayesian Parametric Estimation Based on Computer Vision Measurements

Yun Zhou[1]; Jin-Nan Hu[2]; Guan-Wang Hao[3]; Zheng-Rong Zhu[4]; and Jian Zhang, M.ASCE[5]

Abstract: Conventional methods to identify influence lines, which are essential in design and evaluation of bridges, use contact sensors involving high upfront and operational costs. This paper presents an approach to identifying influence lines based on computer vision measurements. The approach integrates vision-based identification of vehicle types, estimation of vehicle loads, bridge displacement measurement, and Bayesian parametric estimation. A you only look once version 4 (YOLOv4)—a real-time object detector—with a convolutional block attention module is trained to identify vehicle types and estimate vehicle loads. Bridge displacement measurements provide dynamic deflections, which are then used to analyze the influence line through Bayesian parametric estimation. The performance of this approach was evaluated through laboratory and field experiments with different types of vehicles and driving speeds. The results show that the errors were up to 4.88% for laboratory experiments and up to 11.48% for field experiments. This research provides findings that will help with the practices of condition monitoring and assessment of highway bridges. **DOI: 10.1061/JBENF2.BEENG-6235**. © *2023 American Society of Civil Engineers*.

Author keywords: YOLOv4; Convolutional block attention module (CBAM); Target detection; Influence line; Bayesian parametric estimation; Markov chain Monte Carlo.

Introduction

Although condition monitoring and assessment of short- and medium-span bridges plays a critical role in the resilience of the infrastructure network (Kromanis and Kripakaran 2017; Xia et al. 2019), few such bridges are instrumented with health monitoring systems and there is a lack of data that can be used to assess their conditions (Fang et al. 2022). Since the installation of monitoring systems often requires traffic closures that interrupt the transport network (Zheng et al. 2022), there is a need for effective and efficient approaches to bridge condition monitoring that do not affect the operation of the bridge.

Various methods have been developed for the systematic identification and evaluation of bridge structures. However, many ignore the contribution of traffic load to the structural damping, and the mechanical parameters of the vehicles need to be known in advance for some methods (Dan et al. 2022). Advanced approaches that modify sparse component analysis by time-frequency have been developed to improve the accuracy and efficiency of system identification (Yao et al. 2018), as well as optimization of sensor placement solutions using a parallel optimization framework based on a competent genetic algorithm or by using a hypotrochoid spiral optimization algorithm (Wu et al. 2019; Mahjoubi et al. 2020), but they are still affected by the location of sensors and ambient randomness. Other types of sensors have been utilized for structural condition monitoring and assessment of bridges, such as: direct measurements by displacement sensors to assess bridge condition, which involves high price, high cost of manpower and material resources, and is sensitive to environmental factors (Cho et al. 2018); the use of strain gauges and inclinometers to evaluate bridge girder deflections based on polynomial functions (Sousa et al. 2013); the application of distributed fiber optic sensors to bridge strain and deflection profile measurements to provide reliable structural health monitoring of the bridge (Siwowski et al. 2021), but the experimental process of the last two methods requires closed traffic for a long period of time; the use of distributed optical fiber sensors for stiffness monitoring and damage identification of highway bridges under moving vehicle loads (Wu et al. 2017); and the use of long-gauge fiber Bragg grating strain sensors for reference-free damage identification of highway continuous girder bridges (Zhang et al. 2022); however, the practicability of these last two methods requires verification by a real bridge test.

Alternatively, to make bridge structure evaluations cheaper, more convenient, and faster, influence line (IL) testing and extraction can be used. The bridge IL can reflect the displacement, stress, shear, bending moment, and other effects on the structure at a given position due to the imposition of a unit moving load at any position (Belegundu 1988). Therefore, it serves as a significant performance index for condition assessment of bridge structures and has been widely applied to the fields of health monitoring of bridges (Zheng et al. 2019a), such as damage identification (Alamdari et al. 2019; Yang et al. 2022; Zeinali and Story 2018), finite-

[1]Professor, College of Civil Engineering, Key Laboratory for Damage Diagnosis of Engineering Structures of Hunan Province, Key Laboratory of Building Safety and Energy Efficiency of the Ministry of Education, Hunan Univ., Changsha 410082, China. Email: zhouyun05@hnu.edu.cn

[2]Master's Student, College of Civil Engineering, Hunan Univ., Changsha 410082, China (corresponding author). Email: hu1110@hnu.edu.cn

[3]Ph.D. Candidate, College of Civil Engineering, Hunan Univ., Changsha 410082, China. Email: gwh0114@163.com

[4]Ph.D. Candidate, College of Civil Engineering, Hunan Univ., Changsha 410082, China; Changsha Construction Project Quality and Safety Supervision Station, Changsha 410000, China. Email: zrzhu@hnu.edu.cn

[5]Professor, Key Laboratory of Engineering Mechanics of Jiangsu Province, Southeast Univ., Nanjing 210096, China. Email: jian@seu.edu.cn

Note. This manuscript was submitted on December 20, 2022; approved on July 14, 2023; published online on September 18, 2023. Discussion period open until February 18, 2024; separate discussions must be submitted for individual papers. This paper is part of the ***Journal of Bridge Engineering***, © ASCE, ISSN 1084-0702.

element model updating (Liao et al. 2012; Strauss et al. 2012; Xiao et al. 2015), and bridge weigh-in-motion (BWIM) (Zhao et al. 2015; Ojio et al. 2016; OBrien et al. 2018). The difference in deflection of the IL under a symmetrical load was used for damage detection, which is suitable for multidamage and only one deflection sensor is needed in theory (Liu et al. 2012). Chen et al. (2015) proposed a new damage localization technique for a long suspension bridge based on stress ILs, which relies on the weigh-in-motion system. The curvature of noisy static deformation of ILs was used to predict the location and damage severity of the structure, although a significant number of load placement locations might be required (Zeinali and Story 2018). The rotation IL, which relies on rotation measurements obtained from the bridge bearing locations, was used for condition assessment, although the many strain gauge sensors required make it not economically efficient (Alamdari et al. 2019). Ren et al. (2011) proposed a response surface methodology-based model using uniform design and structural static responses, and Xiao et al. (2015) proposed a new model updating method that uses both modal frequencies and multiscale (displacement and stress) static ILs as updating objectives. These two methods have the advantages of easy implementation, high cost-efficiency, and adequate updating accuracy, but they require the bridge closed to traffic and truck weighing in advance. Another important application of the IL is BWIM, which can effectively predict static axle and gross weights (Moses 1979). The IL was taken as a reference in a BWIM system, based on which the axle load effects on bridges (OBrien and Enright 2013) and weights of heavy vehicles (Zhao et al. 2015) were obtained. Deng and Cai (2010) proposed a method for identifying dynamic vehicular axle loads using the superposition principle and influence surface concept. Furthermore, as an alternative approach to conventional BWIM, probabilistic BWIM was proposed to infer axle weights using a probabilistic IL (OBrien et al. 2018). However, the above IL-based BWIM methods have the disadvantages of high price, high cost of manpower and material resources, and being affected by measurement noise.

An IL can be identified in the time domain or the frequency domain. Representative time-domain approaches include, but are not limited to, the matrix method (OBrien et al. 2006), a fitting method based on piecewise polynomial from bridge dynamic response induced by a passing vehicle (Wang et al. 2017), maximum likelihood estimator method by inversing the established calibration vehicle information matrix (Ieng 2015), adaptive B-spline basis dictionary method and the regularized least squares QR decomposition method, which introduced the regularization method into the matrix method to avoid unreasonable fluctuation in the identified influence lines (Chen et al. 2019; Zheng et al. 2019b), and the dynamic fluctuation part elimination method based on empirical mode decomposition (Zheng et al. 2020). The frequency-domain method makes full use of the fact that the Fourier transform of the response of a structure is equal to the point-wise multiplication of the load and the IL in the frequency domain. Frøseth et al. (2017) used the fast Fourier transform (FFT) algorithm to obtain a static IL from measurements and proposed regularization filters in the frequency domain to extract ILs efficiently, while Yan and Yuen (2020) proposed a frequency-domain approach for extracting the IL of a beam-like structure without information on moving loads. The time-domain method is suitable for the problem of IL identification with limited noise, while the frequency-domain method provides an efficient process to identify ILs, but its accuracy is affected by the spectrum leakage problem. Compared to the conventional matrix method in the time domain, the frequency-domain approach effectively reduces the computational complexity of IL identification. Current research mainly employs contact sensors to collect bridge response data for time-domain or frequency-domain analysis. However, there are still many problems, such as the high cost of test equipment, insensitivity to local diseases, being easily affected by environmental changes, and reliance on a BWIM system to obtain axle load information. Installation and operation of sensors involve significant upfront and long-term costs related to time and labor. Most short- and medium-span bridges are not instrumented with these sensors (e.g., displacement sensors, strain gauges, and a BWIM system). With the rapid development of artificial intelligence, machine vision and big data have been gradually integrated with bridge health monitoring technology. Based on the traffic flow video, the speed (Zhang et al. 2019), weights (Zhou et al. 2021a; Dan et al. 2019), real-time position (Chen et al. 2016), type of vehicle (Zhou et al. 2020; Hou et al. 2019; Zhu et al. 2022), and dynamic response information of the bridge structure can be obtained by machine vision and machine learning (Han et al. 2022), which can effectively overcome cost disadvantages. Zhou et al. (2021b) proposed a noncontact technology to identify the IL by constructing the axle weight matrix through interval bounded axle weight values and combining affine arithmetic and support vector machines. However, this method relies on the accuracy of the axle weight value interval, and its application is limited to numerical simulations and laboratory scale tests. Dong et al. (2019) proposed a completely noncontact structural identification system for identifying the IL, which is based on machine vision technology that avoids having to calibrate vehicle axle load. The machine vision method in the context of bridge health monitoring has the characteristics of being a noncontact method, requiring no closure of traffic, and can effectively reduce physical risk. Furthermore, the solution to identifying the IL is a typical inverse problem. Least squares method and regularization method were employed to deal with ill-posedness of inverse problems and produced a reasonable estimate (Rowley et al. 2009). However, the solution to an inverse problem is not a single estimate but a probability distribution. Another approach is statistical inversion based on Bayesian statistics, which reformulates inverse problems as problems of statistical inference. In the statistical method, variables are modeled with an informative or noninformative prior, with the informative prior being a known distribution and the noninformative prior being a random uniform distribution (Kaipio and Somersalo 2006). Therefore, the distribution of the unknowns is generated in the statistical inversion based on Bayesian statistics as the solution of the inverse problem.

Yuen (2010) proposed a Bayesian probabilistic framework for structural model updating using input–output measurements, which overcomes the uncertainty caused by finite information of the data. Beck (2010) utilized probability logic with Bayesian updating to quantify modeling uncertainty and perform system identification, which was regarded as an inference to plausible system models. A Bayesian fast Fourier transform approach (BFFTA) was presented to obtain the optimal values of the updated modal parameters and their associated uncertainties (Yuen and Katafygiotis 2003). Au (2011) investigated the determination of the posterior covariance matrix of modal parameters within the framework of a BFFTA for modal identification using ambient vibration data. Au and Ni (2014) developed a Bayesian approach that properly accounted for uncertainty in accordance with probability logic for modal identification. Zhang et al. (2015) investigated the posterior uncertainty of modal parameters in terms of their covariance matrix, which was verified by laboratory data. Sun et al. (2015) presented a Bayesian time-domain method to identify structural parameters and unknown input loads using incomplete output measurement only (acceleration and dynamic strain). Argyris et al. (2020) proposed modal-based Bayesian model-updating

methodology regarding inclusion of the mode shapes. The relationship between dynamic response and IL was embedded in Bayesian inference framework by Yan and Yuen (2020), which has the advantage of avoiding the ill-posedness nature of inverse problems. However, the achievement of this method relied on the reference IL, of which the application was limited to numerical studies. A review of relevant literature reveals that Bayesian statistics has been widely applied in model updating and parameters estimation.

In Bayesian statistics, the randomness of parameters describes the uncertainty of information, and the external data are utilized for parameter updating. Furthermore, it can overcome pathological solution and the ill-posedness nature of inverse problems. However, few scholars have applied statistical inference to solve the posterior distribution of IL, which is in the category of structural parameters. In addition to this, most of the time and frequency domain methods for identifying influence lines require known accurate bridge response (outputs) and vehicle information (inputs, e.g., axle distance and axle weight) (Zheng et al. 2019a). However, Bayesian theory can solve IL identification in the absence of a BWIM system (only partial vehicle information is known) by statistical inference. To propose an automatically identifying IL method for highway bridges using Bayesian parametric estimation based on computer vision, this study first establishes a machine vision-based vehicle target identification and classification method, then combines the established vehicle data and information database to obtain partial vehicle parameter information (virtual axle weight matrix), and finally proposes an IL identification method based on Bayes' theorem. The method has the advantages of not relying on a BWIM system (without the need to obtain accurate vehicle axle load intervals and axle spacing), and only requires the response of the bridge measurement location, combined with the vehicle parameter information obtained from the video identification to obtain the displacement IL. Furthermore, the method does not require interruption of normal traffic flow.

Motivated by the existing development of machine vision and Bayesian statistics, this paper proposes an approach to identify IL of bridges based on computer vision measurements and machine learning. Compared with existing research, the novelty of this research is that the proposed approach integrates identification of vehicle types, estimation of vehicle loads, bridge vibration measurement, and Bayesian parametric estimation. Based on machine vision technology, a YOLOv4 with convolutional block attention module (CBAM) is developed to identify vehicle types, followed by estimation of vehicle information. Furthermore, bridge vibration measurement provides dynamic deflections by computer vision measurements, which are then utilized to analyze the IL of bridges through Bayesian parametric estimation. This process does not rely on a BWIM system and does not require closing the bridge to traffic. The performance of the proposed approach was evaluated through numerical simulations, laboratory tests, and field experiments with several conditions, different types of vehicles, and driving speeds. Additionally, the proposed method is compared with the IL identification algorithm based on interval analysis with affine arithmetic (AAIL) proposed by the authors in previous research (Zhou et al. 2021b) in the field tests section to further demonstrate the efficiency of the proposed method presented in this paper. The findings from this research will help with practices in condition monitoring and assessment of highway bridges.

The remainder of the paper is organized as follows: Section "Methods" elaborates the proposed methods. Sections "Numerical simulations," "Laboratory Tests," and "Field Tests" introduce the numerical simulations, laboratory tests, and field tests, respectively. And the Section "Conclusions" summarizes the conclusions and provides suggestions for future related research.

Methods

Overview

Fig. 1 shows the framework of the proposed approach with four interconnected modules, which are utilized to identify vehicle types (Module 1), estimate vehicle loads (Module 2), measure bridge displacement responses (Module 3), and estimate IL (Module 4). Module 1 ["Identification of Vehicle Types (Module 1)" section] identifies vehicle types using a YOLOv4 with CBAM, which is

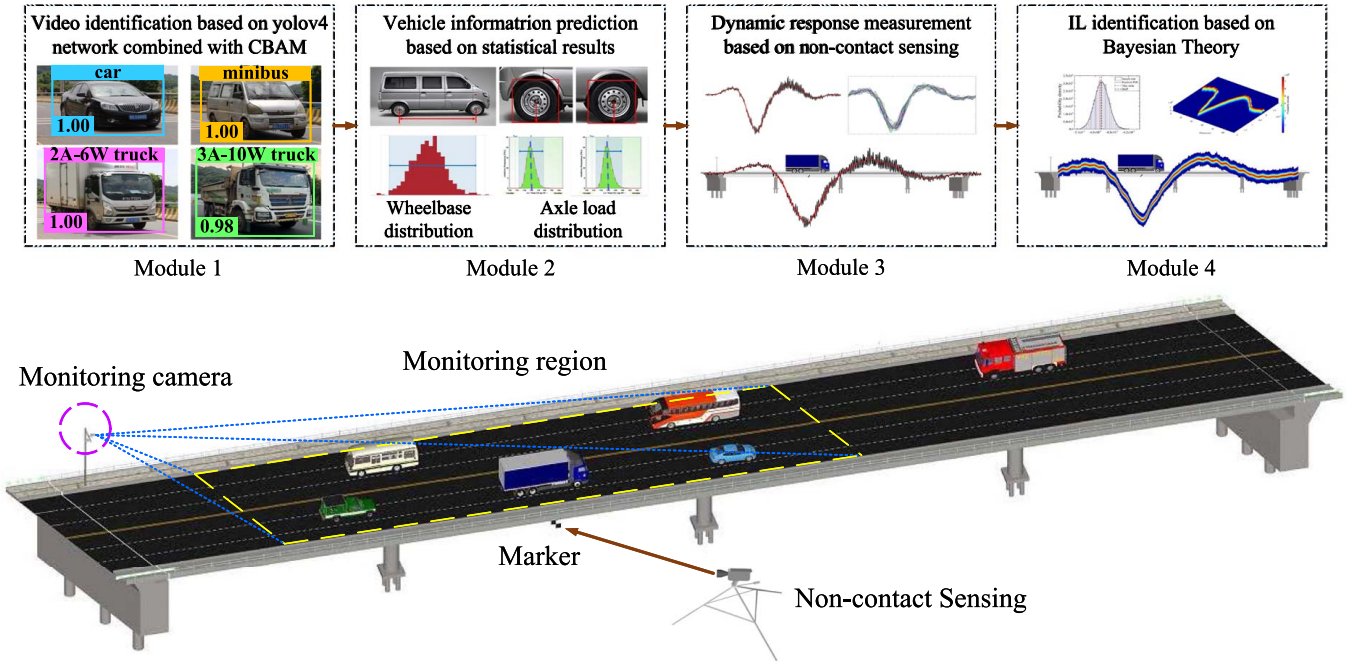

Fig. 1. Framework of the IL identification system.

J. Bridge Eng., 2023, 28(12): 04023087

trained using photos of various types of vehicles such as two-axle and three-axle vehicles. Module 2 ["Estimation of Vehicle Loads (Module 2)" section] estimates the weight and axle spacing of vehicles, which are already identified by Module 1, based on statistical data collected from prior research (Zhou et al. 2020). Module 3 ["Measurement of Bridge Displacements (Module 3)" section] measures the displacement responses of bridges based on a computer vision approach. Module 4 ["Identification of Influence Lines (Module 4)" section] estimates the IL based on the vehicle loads estimated in Module 2 and the bridge vibrations measured in Module 3, using the Efficient No-U-Turn Sampler (E-NUTS) based on Bayesian theory (Hoffman and Gelman 2014). The four modules are elaborated on in the following subsections. Additionally, the numerical simulations and laboratory tests on vehicle–bridge coupling vibration first verified that Module 4 can effectively identify the IL of the bridge structure based on the response of multiple load cases and the corresponding virtual axle weights. Furthermore, the field experiments verified the effectiveness of the overall framework of the proposed approach for different driving speeds and different vehicle types.

Identification of Vehicle Types (Module 1)

Identification of vehicle types is performed using a YOLOv4 with CBAM, as shown in Fig. 2. YOLOv4 was selected due to its high efficiency and accuracy shown in previous studies (Tang et al. 2020; Chen et al. 2022). The YOLOv4 includes four primary parts: CSPDarknet53, Spatial Pyramid Pooling, Path Aggregation Network, and Yolo Head (Bochkovskiy et al. 2020). The CSP module in CSPDarkNet53 can improve the learning ability of the convolutional network and ensure the detection accuracy while reducing the computational effort. YOLOv4 uses the MISH activation function as the activation function in CSPDarkNet53, and the rest still use the LeakyReLU function. Meanwhile, YOLOv4 uses spatial pyramid pooling and path aggregation network (PANet), allowing the algorithm to adapt to images of different resolutions and enhance the instance segmentation process by preserving spatial information. Finally, to improve the speed and accuracy of identification, YOLOv4 uses three different scale feature maps of 19×19, 38×38, and 76×76 to predict the detection results.

CBAMs are added to increase the weight of the region of interest (ROI), which is the region with vehicles, while suppressing the weights of regions without vehicles. The use of CBAM is expected

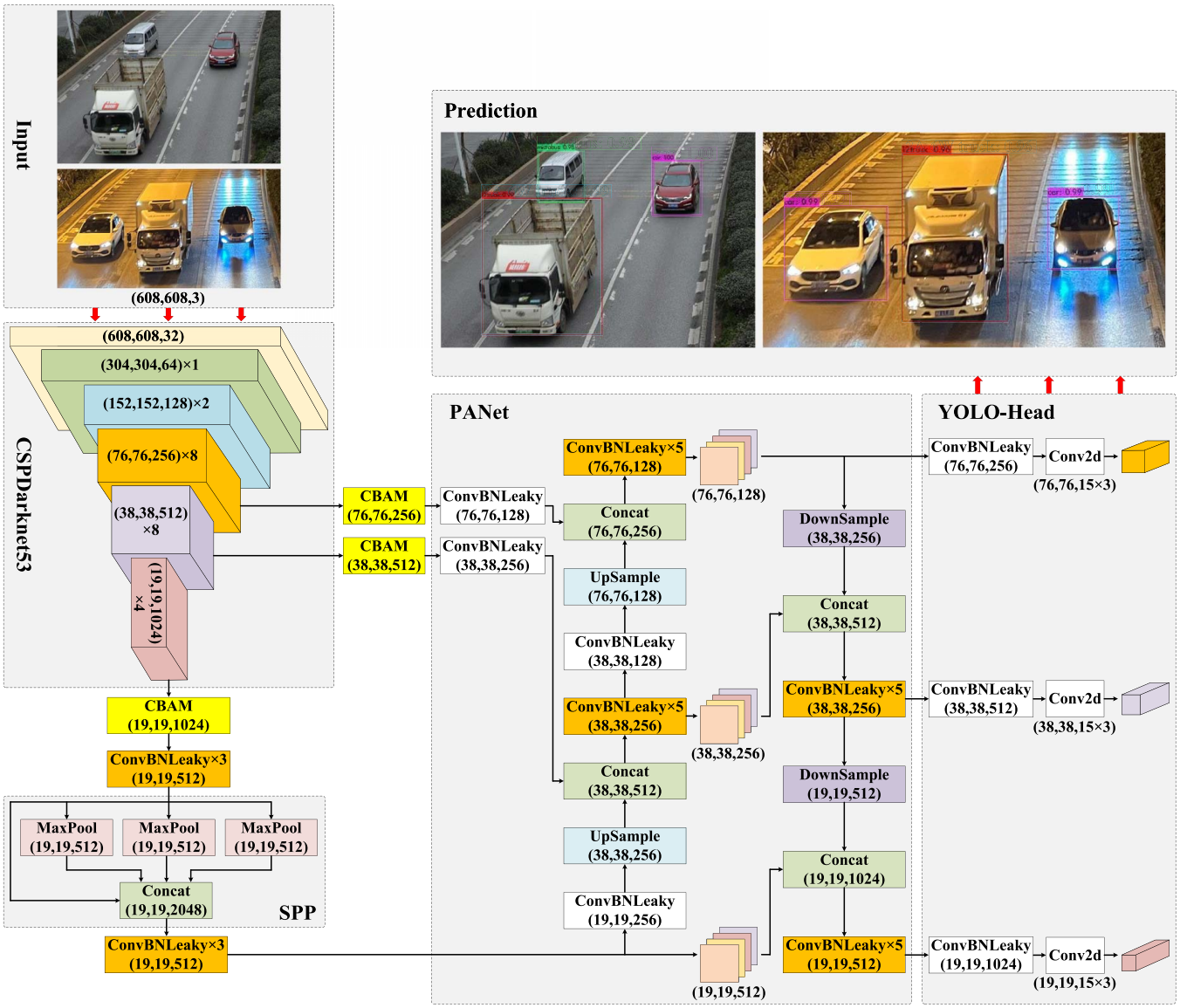

Fig. 2. YOLOv4-CBAM network.

to increase the efficiency and accuracy of identification of vehicle types. The CBAM is composed of a channel attention mechanism and a spatial attention mechanism (Woo et al. 2018). The channel attention mechanism generates masks and evaluation scores, which are utilized to achieve the weighted processing of input images, as shown in Eqs. (1) and (2):

$$M_c(F) = \sigma(\text{MLP}(\text{AvgPool}(F)) + \text{MLP}(\text{MaxPool}(F))) \quad (1)$$

$$F' = M_c(F) \otimes F \quad (2)$$

The spatial attention mechanism improves the efficiency and accuracy by inputting weight coefficients and obtaining the product of weight coefficients and the information, as shown in Eqs. (3) and (4):

$$M_s(F') = \sigma(f^{7\times7}([\text{AvgPool}(F'); \text{MaxPool}(F')])) \quad (3)$$

$$F'' = M_s(F') \otimes F' \quad (4)$$

where F = input feature map; $M_c(F)$ = channel attention map output by the channel attention module; F' = output feature map of the channel attention module; MLP = multilayer perceptron; $M_s(F')$ = spatial attention map output by the spatial attention module; F'' = feature map output by the CBAM; AvgPool and MaxPool = channel-based global average pooling and global maximum pooling, respectively; σ = sigmoid function; $f^{7\times7}$ = convolution operation with the filter size of 7×7; and $\otimes$ = element-wise multiplication.

Mosaic data augmentation is used to augment the training data. Four images are randomly selected from the original database, modified by a series of operations (e.g., clipping and zooming), and combined into one image. The data augmentation is expected to improve the robustness of the trained YOLOv4 model. Batch normalization is used to calculate activation statistics from four different images on each layer, which eliminates the necessity of using a large mini-batch size (Bochkovskiy et al. 2020).

Based on the team's previous research (Zhou et al. 2020), a detailed reclassification of two-axle and three-axle trucks was performed. Further, rough-grained classification criteria were proposed to classify common vehicles into 10 types, which are sedan car, mini bus, light truck, large truck, coach truck, two-axle truck with 4 wheels (2A–4W truck), two-axle truck with 6 wheels (2A–6W truck), three-axle truck with 8 wheels (3A–8W truck), three-axle truck with 10 wheels (3A–10W truck), and four-axle truck with 12 wheels (4A–12W truck), as shown in Fig. 3.

To evaluate the influence of illumination conditions and vehicle speeds on the detection accuracy, images were collected during the day and at night. More than 1,000 images were collected for each type of vehicle to form a data set, which was split into training and testing sets with a ratio of 8:2 to ensure the identification accuracy of the model and to have enough data sets to test the trained model (Wang et al. 2021; Zhou et al. 2020; Cheng et al. 2022). The convergence curves of the training process for YOLOv4 and YOLOv4 with CBAM are plotted in Fig. 4. The bottom and top lines represent the training loss and AAP result, respectively. The identification accuracy of the improved YOLOv4 with CBAM is slightly improved, and the fluctuation of AAP during model training is significantly reduced. YOLOv4 with CBAM (0.018 s) has less processing time for a single image compared to YOLOv4 (0.047 s). With the testing set, the identification accuracies of YOLOv4 with CBAM for images collected by unmanned aerial vehicle (UAV) during the day and at night were more than 98% and 96%, respectively, indicating that the trained YOLOv4 with CBAM has high accuracy. The definition of AAP is given in

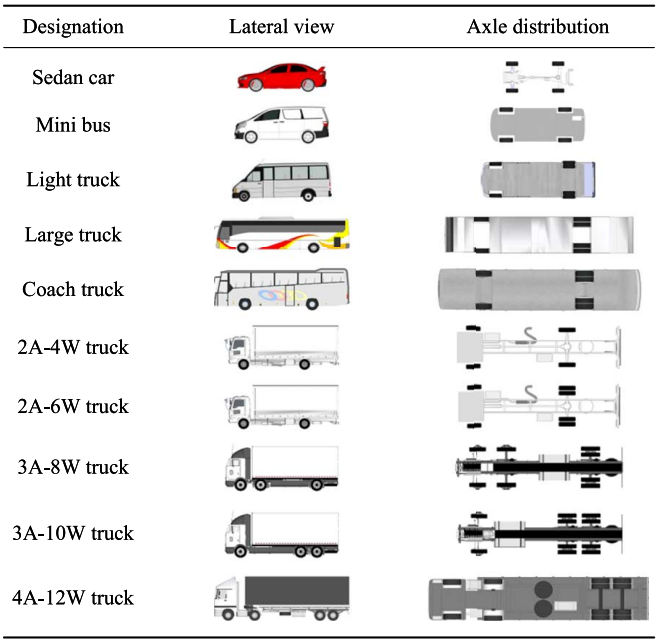

Fig. 3. Illustration of the considered types of vehicles.

Eq. (5), which is a performance metric used to evaluate the accuracy of the trained YOLOv4 model:

$$\text{AAP} = \frac{\sum_{i=1}^{G} \int_0^1 P(R)dR}{G} \quad (5)$$

where AAP = average accuracy of all categories, which can measure the performance of the model in all categories; and G = number of detected categories. AP is usually used as a criterion to evaluate the performance of an object detection model. It represents the accuracy of the model in a certain category, and is the area enclosed by the precision–recall (P-R) curve (with recall as x-axis and precision as y-axis). The calculation formulas for precision rate and recall are as follows (Fu et al. 2021):

$$\text{Precision} = \frac{\text{TP}}{\text{TP} + \text{FP}} \quad (6)$$

$$\text{Recall} = \frac{\text{TP}}{\text{TP} + \text{FN}} \quad (7)$$

where TP = number of positive samples correctly predicted; FP = number of negative samples incorrectly predicted; and FN = number of positive samples incorrectly predicted.

Estimation of Vehicle Loads (Module 2)

A data set containing 5,123 records was established by collecting parameters from websites for the classified trucks after reclassification of two-axle and three-axle trucks. Among them, each message includes axle spacing, axle load distribution coefficient, curb weight (minimum value of the sum of all axle loads of the vehicle), and maximum permissible total weight (maximum value of the sum of all axle loads of the vehicle) of the truck, as shown in Fig. 5 and Table 1. Based on the vehicle types identified and classified by the model, the mapping relationship between the vehicle types and their corresponding vehicle parameter information is obtained in combination with the vehicle data and information base established.

Measurement of Bridge Displacements (Module 3)

The video displacement system (VDS) developed by Yan et al. (2021) includes a video acquisition device, a lighting device, and a video image processing system. The VDS has been used for dynamic displacement measurements due to its long-distance multipoint noncontact test, simple equipment, easy implementation, and higher testing accuracy (Liu et al. 2022; Yan et al. 2021). In this study, the video displacement system was used to measure the midspan displacement responses of bridges in field tests based on the digital image correlation technique that combines the Fourier transform-based cross correlation (FTCC) integer-pixel registration algorithm and the inverse compositional Gauss–Newton (IC-GN) subpixel registration algorithm (Reddy and Chatterji 1996; Pan et al. 2013).

Since the accuracy of VDS deformation measurement is positively correlated with the length that can be represented by a pixel point in a video image, subpixel means that the pixel is subdivided so that the subpixel can represent a smaller length. Therefore, to achieve relatively higher accuracies in displacement time-history measurements, it is necessary to provide acceptable subpixel resolution accuracy in the displacement time-history domain. First, a vision sensor system composed of a high-speed video camera and computer processing system is employed to capture the image sequences including the selected ROI with an existing surface feature. Second, the integer-pixel image registration algorithm FTCC uses the overlap region between the referenced subset $t(x, y)$ and the current subset $g(x, y)$ to be matched to invert the mutual power spectrum in its frequency domain to obtain the impulse function. Third, by detecting the peak position of the function, the detection of the two-dimensional displacement of the image in the null domain is achieved. From this, an accurate initial guess for the deformed images is achieved based on the iterative initial values provided by the integer-pixel registration algorithm FTCC. Further, a novel subpixel registration algorithm IC-GN with a higher registration accuracy and efficiency is used to converge this integer-pixel initial value to a local optimal solution at the subpixel level to track the selected ROI with existing surface features from the image sequence, thereby achieving deformation measurement at the subpixel level (Yan et al. 2021).

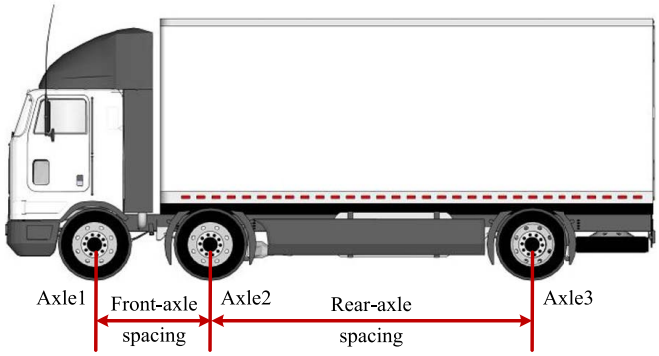

Fig. 5. Vehicle parameters of the 3A–8W truck.

Identification of Influence Lines (Module 4)

Mathematical Model of IL

When a calibration vehicle with known axle weight W_i and known axle distance D_i passes over a bridge, it results in a series of measurements of the load effect y_k^T (Zheng et al. 2019b). Assuming linearity (Zheng et al. 2022), the response generated by multiple external excitations caused by the vehicle are a summation of the effect of each individual excitation of each individual axis of the vehicle (Zaurin and Catbas 2010a, b). Hence, for each sampling point k, the vehicle-induced responses y_k^T can be expressed through the axle weight W_i and the influence coefficient of the bridge $I_{(k-C_i)}$ corresponding to the ith axle (OBrien et al. 2006; Zheng et al. 2019b):

$$y_k^T = \sum_{i=1}^{Q} W_i I_{(k-C_i)} \tag{8}$$

$$C_i = \frac{D_i f}{v} \tag{9}$$

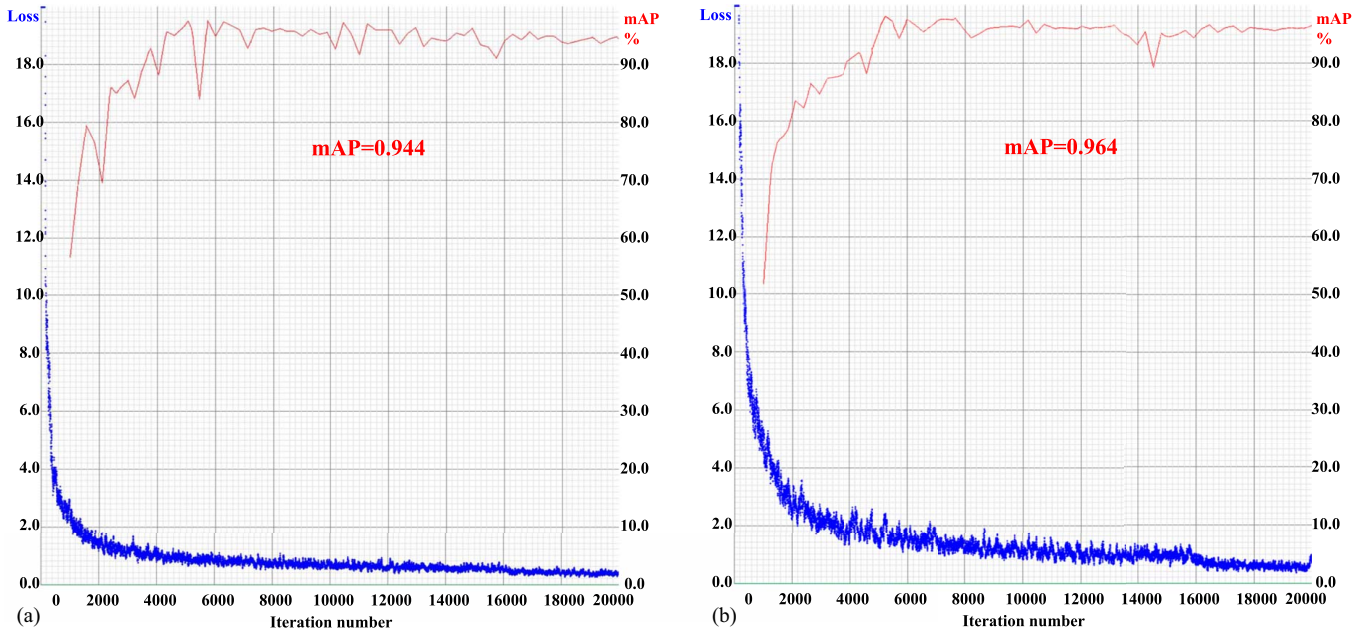

Fig. 4. Training results: (a) YOLOv4; and (b) YOLOv4-CBAM.

Table 1. Distribution interval of vehicle parameters

Vehicle type	Axle spacing (mm)		Overall weight (kg)	Axle load distribution coefficient		
	Front-axle spacing (min., max.)	Rear-axle spacing (min., max.)	(min., max.)	Axle 1 (min., max.)	Axle 2 (min., max.)	Axle 3 (min., max.)
2A–4W truck	(2,000, 3,450)	—	(700, 3,470)	(0.28, 0.53)	(0.47, 0.72)	—
2A–6W truck	(2,300, 5,800)	—	(1,400, 18,000)	(0.25, 0.51)	(0.49, 0.75)	—
3A–8W truck	(1,700, 2,000)	(2,500, 6,000)	(6,700, 25,500)	(0.19, 0.30)	(0.19, 0.30)	(0.40, 0.62)
3A–10W truck	(2,925, 5,950)	(1,300, 1,450)	(7,460, 25,450)	(0.24, 0.50)	(0.25, 0.38)	(0.25, 0.38)

Note: Overall weight is the sum of all axle loads of the vehicle, and the axle loads distribution coefficient is the ratio of axle loads to global weight of each axle. The 2A–4W truck and 2A–6W truck indicate a two-axle truck total with 4 and 6 wheels, respectively. The 3A–8W truck and 3A–10W truck indicate a three-axle truck total with 8 and 10 wheels, respectively.

where Q = number of vehicles axles; C_i = sampling point difference between the first axle and the ith axle; D_i = axle spacing; f = sampling frequency; and v = vehicle velocity. Fig. 6 illustrates the decomposition process of the unit IL.

Eq. (8) can be rewritten in a matrix form as follows (Zheng et al. 2022):

$$\{Y\}_{K,1} = [W]_{K,K-C_Q}\{I\}_{K-C_Q,1} \tag{10}$$

or

$$\begin{Bmatrix} y_1^T \\ y_2^T \\ \vdots \\ y_K^T \end{Bmatrix}_{K\times 1} = \begin{bmatrix} W_1 & 0 & \cdots & 0 \\ 0 & W_1 & & \vdots \\ \vdots & 0 & \ddots & 0 \\ W_2 & \vdots & & W_1 \\ 0 & W_2 & & 0 \\ \vdots & 0 & \ddots & \vdots \\ W_Q & \vdots & & W_2 \\ 0 & W_Q & & 0 \\ \vdots & \vdots & \ddots & \vdots \\ 0 & 0 & \cdots & W_Q \end{bmatrix}_{K\times(K-C_Q)} \times \begin{Bmatrix} I_1 \\ I_2 \\ \vdots \\ I_{K-C_Q} \end{Bmatrix}_{K-C_Q\times 1} \tag{11}$$

where $\{Y\}_{K,1}$ = responses vector collected at each time step; $[W]_{K,K-C_Q}$ = axle load matrix containing the vehicle information of axle load and axle number; and $\{I\}_{K-C_Q,1}$ = vector consisting of the bridge IL ordinate.

In addition, K is the sampling number of measurements, which can be expressed as follows:

$$K = \frac{(L + D_Q)f}{v} \tag{12}$$

where L = length of the bridge; and D_Q = distance from Axle-1 to Axle-Q.

The aforementioned method is established with the acknowledgment of known input and output. The dynamic responses (output information) of the bridge under moving vehicles should be accurately measured. In addition, it is necessary to preweigh the calibrated vehicle to obtain the vehicle load information (i.e., type, axle load, motion speed, and axle spacing) and thereby determine the corresponding elements of the matrix $[W]$ (input information). This method is not suitable for the structural health monitoring of small- and medium-span bridges without a BWIM system. However, Bayesian theory can achieve the identification of bridge ILs (unknown parameters) in the absence of a BWIM system by combining the dynamic response of the bridge under moving vehicles with partial load information of the corresponding vehicle (virtual axle load matrix).

Bayesian Inference

This study uses Bayesian inference to estimate unknown parameters, which are θ_1, θ_2, …, θ_n. The posterior distribution is given by (Yuen 2010)

$$p(\theta|\psi) = \frac{p(\psi|\theta)p(\theta)}{\int_\Theta p(\psi|\theta)p(\theta)d\theta} \tag{13}$$

where θ = parameter to identify; $p(\theta|\psi)$ = posterior distribution of the parameters; ψ = observed data; $p(\theta)$ = prior distribution of parameters; and $p(\psi|\theta)$ = the likelihood function:

$$p(\psi|\theta) = L(\theta|\psi_1, \psi_2, \ldots, \psi_n) = \prod_{i=1}^{n} p(\psi_i|\theta) \tag{14}$$

where $p(\psi_i|\theta)$ = probability density function (PDF); ψ_i = value of the ith observation; and n = number of observations.

In Bayesian statistics, the prior distribution represents known knowledge of unknown parameters (e.g., IL ordinate). The prior distribution includes informative and noninformative prior

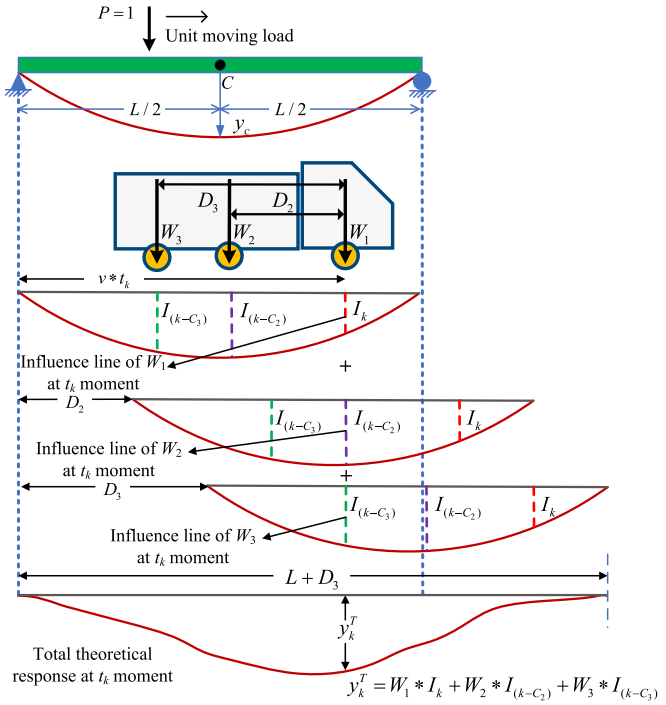

Fig. 6. Unit IL decomposition.

distributions. Informative prior distribution is established based on prior knowledge, which is usually obtained from professional knowledge and expert experience. When there is limited prior knowledge about the unknown parameters, a noninformative prior distribution can be adopted. In this study, the noninformative prior distribution is used because the information of the IL parameters is unknown. A uniform distribution or a normal distribution with a large variance can be chosen as the noninformative prior distribution. The noninformative prior distribution contains little information and does not influence the posterior distribution. In this case, the statistical inference will rely solely on the likelihood of the data (Yuen 2010; Ojo et al. 2017; Wesner and Pomeranz 2021).

Bayesian Parametric Estimation

This section proposes the general Bayesian framework for model parameters updating, by input–output system measurement. A linear or nonlinear dynamical system considering the input–output relationship can be written as follows (Yuen 2010; Zheng et al. 2020):

$$x(t) = \varphi(t, F_{in}, x(0), \theta_m) \tag{15}$$

where φ = relationship between model response output vector $x(t) \in \mathbb{R}^{N_d}$ and input F_{in} at time t; $x(0)$ = initial condition of the model; and θ_m = model parameters.

Assume that response data are available at $N_0 (\ll N_d)$ observed degrees of freedom (DOFs) and Δt denotes the sampling time step, where N_0 denotes the number of observed DOF and N_d represents the sum of the number of degrees of freedom in the dynamical system $x(t)$ (Yuen 2010). The prediction error ε is a combined effect of measurement noise and modeling error. Hence, the measured response $y_n \in \mathbb{R}^{N_0}$ (at time $t = n\Delta t$) will be different from the model response $L_0 x(n\Delta t)$ corresponding to each DOF. L_0 is defined as the transfer matrix representing the input–output relationship of the system, which is an observed matrix of $N_0 \times N_d$.

$$y_n = L_0 x(n\Delta t) + \varepsilon_n \tag{16}$$

where ε is modeled as a discrete zero-mean Gaussian white noise vector ($\varepsilon_n \in \mathbb{R}^{N_0}$), and it satisfies the following correlation structure:

$$E[\varepsilon_n \varepsilon_{n'}^T] = \sum\nolimits_{\varepsilon} \delta_{nn'} \tag{17}$$

where $E[\cdot]$ = expectation; $\delta_{nn'}$ = Kronecker delta function; and $\sum_{\varepsilon} = N_0 \times N_0$ covariance matrix of the prediction error process.

To reduce computational complexity and ensure that the prediction errors do not affect each other and are noninformative, assuming the prediction errors of different channels of measurements have equal variances and stochastic independence, the covariance matrix of prediction errors is (Yuen 2010)

$$\sum\nolimits_{\varepsilon} = \sigma_{\varepsilon}^2 I_{N_0} \tag{18}$$

where $I_{N_0} = N_0 \times N_0$ identity matrix.

The likelihood function $p(D|\theta, C)$ given dynamic data D and Model class C, may be expressed as follows:

$$p(D|\theta, C) = (2\pi)^{-NN_0/2} \sigma_{\varepsilon}^{-NN_0} \exp\left[-\frac{NN_0}{2} J_g(\theta_m; D, C)\right] \tag{19}$$

where the dynamic data D consists of the measured time histories of the excitation and system response. The uncertain parameter is denoted as θ, which includes the model parameters θ_m and the diagonal element of $\sum_{\varepsilon}$.

After the parameter $\theta = [\theta_m^T, \sigma_{\varepsilon}^2]^T$ is updated, the posterior PDF is given by

$$p(\theta|D, C) = k_0 p(\theta|C)(2\pi)^{-NN_0/2} \sigma_{\varepsilon}^{-NN_0} \exp\left[-\frac{NN_0}{2} J_g(\theta_m; D, C)\right] \tag{20}$$

where k_0 = normalizing constant; and $p(\theta|C)$ = prior PDF of the uncertain parameters in θ. The goodness-of-fit function is given by

$$J_g(\theta_m; D, C) = \frac{1}{NN_0} \sum\nolimits_{n=1}^{N} \|y_n - L_0 x(n\Delta t; \theta_m, C)\|^2 \tag{21}$$

where $x(n\Delta t; \theta_m, C)$ = model response based on the assumed class of models and the parameter vector θ_m; y_n = measured response at time $n\Delta t$; and $\|\cdot\|$ = Euclidean norm of a vector. Based on the posterior PDF $p(\theta|D, C)$, various statistics can be analyzed for uncertain parameters.

Posterior Distribution of Parameters

It is a challenging task to calculate the statistics characteristics of the posterior PDF since it has a complex topological structure. The Markov chain Monte Carlo (MCMC) technique was used to obtain the statistics of the posterior distributions with accuracy (Andrieu et al. 2003). For complicated models with many parameters commonly encountered in Bayesian inference and statistical physics, common MCMC algorithms such as Gibbs sampling or Metropolis Hastings usually exhibit random walk behaviors that suffer from the problem of inefficiency of parameter space exploration (Neal 1992, 1998). Given that No-U-Turn Sampler (NUTS) avoids inefficient exploration of the parameter space, it can converge to the target posterior distribution quicker than common random walk MCMC algorithms and is, therefore, less computationally expensive. This study utilized E-NUTS to generate MCMC samples from the posterior distribution of the parameters of a Bayesian model (Hoffman and Gelman 2014). The sampling procedure is described as follows:

- *Step 1.* Assign initial values to Markov chain samples: $\{\theta_1^0, \theta_2^0, \ldots, \theta_h^0\}$, where h is the number of parameters.
- *Step 2.* Generate t values ($t = 1, 2, \ldots, T$) until the convergence is achieved.

$$\theta_1^t \sim p(\theta_1|\theta_2^{t-1}, \theta_3^{t-1}, \ldots, \theta_h^{t-1}, D, C)$$

$$\theta_2^t \sim p(\theta_2|\theta_1^t, \theta_3^{t-1}, \ldots, \theta_h^{t-1}, D, C)$$

$$\ldots$$

$$\theta_j^t \sim p(\theta_j|\theta_1^t, \theta_2^t, \ldots, \theta_{j-1}^t, \theta_{j+1}^{t-1}, \ldots, \theta_h^{t-1}, D, C)$$

$$\ldots$$

$$\theta_h^m \sim p(\theta_h|\theta_1^t, \theta_2^t, \ldots, \theta_{h-1}^t, D, C)$$

To reduce the influence of the initial samples on the Markov chain, the first k' samples have been cutoff to ensure that the generated samples satisfy the posterior PDF $p(\theta|D, C)$. In this study, the first 1,000 samples have been cutoff (Hoffman and Gelman 2014). The Markov chain samples $\{\theta_1, \theta_2, \ldots, \theta_h\}$ with PDF approaching $p(\theta_1, \theta_2, \ldots, \theta_h|D, C)$ can be obtained, where $\theta_1 = \{\theta_1^{k+1}, \theta_1^{k+2}, \ldots, \theta_1^T\}$.

A specified number of samples obeying a complex posterior distribution can be generated from the defined Bayesian model by means of E-NUTS. The parameter estimation based on Bayes' theorem is shown in Fig. 7.

Identification Model

A method based on Bayes' theorem is proposed to identify the IL without relying on a BWIM system to obtain accurate vehicle information (e.g., axle distance and axle weight). Bridge dynamic displacement data (Module 3, output) and vehicle parameters

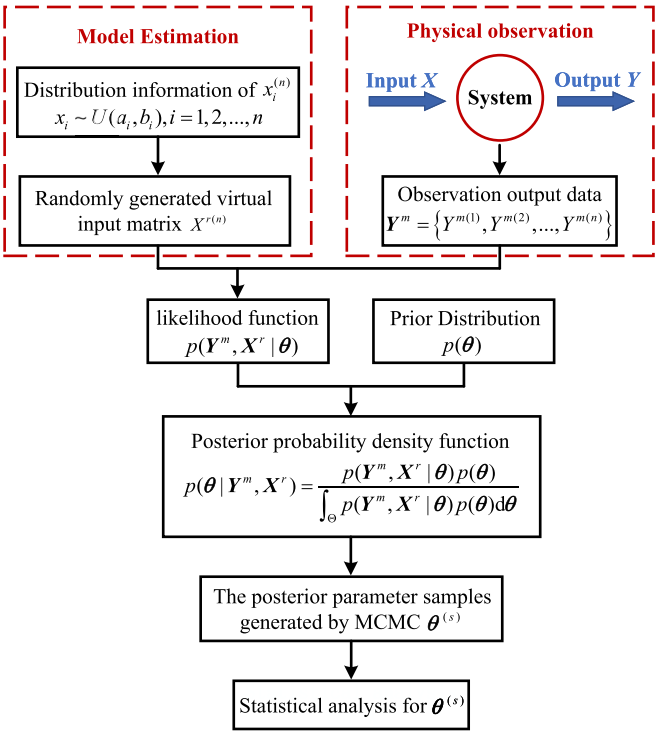

Fig. 7. Parameter estimation flow chart.

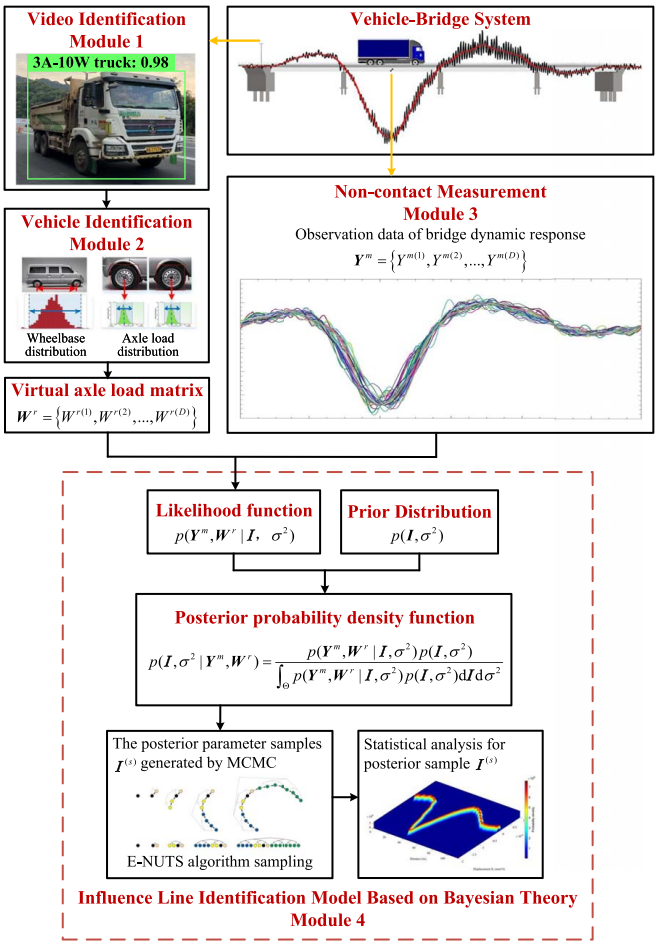

Fig. 8. The flow chart for the identification of IL of bridges.

(Module 2, input) are obtained using the vision-based method. The vehicle types are classified accurately (Module 1), and the vehicle weight and distribution coefficient of axle load are obtained from the Section "Estimation of Vehicle Loads (Module 2)". The inversion model (Module 4) of IL is built to obtain the posterior PDF based on the Bayesian parametric estimation method in the Sections "Bayesian Inference," "Bayesian Parametric Estimation," and "Posterior Distribution of Parameters." The flow chart is shown in Fig. 8.

The vision-based method for bridge displacement response monitoring is prone to noises such as camera jitter. Based on Eq. (10), the multivariate linear relationship after introducing the error vector $\varepsilon^m = [\varepsilon_1^m, \varepsilon_2^m, \ldots, \varepsilon_K^m]^T$ is shown as follows:

$$Y^m = W^r I + \varepsilon^m \tag{22}$$

where the virtual input data W^r corresponding to the output of dynamic response are randomly generated. The displacement response vector $Y^{m(j)} \sim N_K(W^{r(j)} I, \sum_K)$ and error vector $\varepsilon^m \sim N_K(0, \sum_K)$ are obtained through the linear relationship based on the multivariate normal distribution probability model.

With a large amount of bridge displacement data $\{Y^{m(1)}, Y^{m(2)}, \ldots, Y^{m(j)}\}$ (bridge displacement data collected at each case in the test) and corresponding virtual input data $\{W^{r(1)}, W^{r(2)}, \ldots, W^{r(j)}\}$, the likelihood function can be expressed as follows:

$$L(I, \sigma_\varepsilon^2 | Y^m, W^r) = p(Y^m, W^r | I, \sigma_\varepsilon^2) = (2\pi)^{-KE/2} \left| \sum\nolimits_K \right|^{-E/2} \exp\left\{ -\frac{1}{2} \sum\nolimits_{j=1}^{E} (Y^{m(j)} - W^{r(j)} I)^T \sum\nolimits_K^{-1} (Y^{m(j)} - W^{r(j)} I) \right\} \tag{23}$$

where E = number of bridge response conditions included in the calculation.

In the framework of Bayesian parametric estimation, the prior distribution of the parameters $I = [I_1, I_2, \ldots, I_{K-C_Q}]^T$ and σ_ε^2 are defined. Since these parameters are independent of each other, the joint prior distribution is expressed as follows:

$$p(I, \sigma_\varepsilon^2) = \prod_i^{K-C_Q} p(I_i) p(\sigma_\varepsilon^2) \tag{24}$$

Considering the unknown parameters for estimation without any prior knowledge, the noninformative prior is adopted, which is defined as follows:

$$I_i \sim N(0,100),\ i = 1, 2, \ldots, K - C_Q \tag{25}$$

$$\sigma_\varepsilon^2 \sim IGam(0.001, 0.001) \tag{26}$$

The aforementioned setting of I and σ_ε^2 reflects the ignorance of prior knowledge of unknown parameters. N (0,100) represents the normal distribution with mean 0 and variance 100. This is set to ensure that the range of the bridge IL ordinate prior distribution is large enough to effectively contain the true value of the bridge IL ordinate and does not influence the posterior distribution (Ojo et al. 2017; Wesner and Pomeranz 2021). To ensure the random effect of the error, the default noninformative prior distribution *IGam* (0.001, 0.001) is chosen for σ_ε^2 (Gelman 2006; Klein and Kneib 2016). *IGam* (0.001, 0.001) represents the inverse gamma distribution with shape parameter 0.001 and scale parameters 0.001. The Bayesian parameter estimation results are mainly affected by the likelihood function when there are sufficient data. The influence of prior distributions can be ignored.

According to Bayes' theorem, the joint posterior PDF of I and σ_ε^2 can be expressed by the likelihood function and joint prior

distribution, as follows:

$$p(I, \sigma_\varepsilon^2|Y^m, W^r) = \frac{p(Y^m, W^r|I, \sigma_\varepsilon^2)p(I, \sigma_\varepsilon^2)}{\int_\Theta p(Y^m, W^r|I, \sigma_\varepsilon^2)p(I, \sigma_\varepsilon^2)dId\sigma_\varepsilon^2} \tag{27}$$

The marginal posterior PDF of the IL ordinate of an arbitrary point i on the bridge can be obtained by the derivation of the joint posterior PDF of parameters to be identified:

$$p(I_i|Y^m, W^r) = \int_{\Theta_{I_2}}\int_{\Theta_{I_3}}\cdots\int_{\Theta_{I_{K-C_Q}}}\int_{\Theta_{\sigma^2}} p(I, \sigma_\varepsilon^2|Y^m, W^r) \\ dI_1dI_2\ldots dI_{i-1}dI_{i+1}\ldots dI_{K-C_Q}d\sigma_\varepsilon^2 \tag{28}$$

The maximum a posteriori (MAP) I_i^{MAP} of the ordinate of IL can be obtained by

$$I_i^{\text{MAP}} = \arg\max_{I_i} p(I_i|Y^m, W^r) \tag{29}$$

The calculation of the marginal posterior PDF involves a high-dimensional multivariate integral formula. The MCMC algorithm is utilized to estimate the marginal posterior PDF of the IL ordinate by extracting random samples from the joint posterior PDF [Eq. (27)] via E-NUTS sampling.

Numerical Simulations

Vehicle–Bridge Coupled System

The feasibility and accuracy of the proposed method are verified by the numerical test of vehicle–bridge coupling vibration analysis. The equation of motion for a bridge is expressed as follows:

$$[M_b]\{\ddot{Y}_b\} + [C_b]\{\dot{Y}_b\} + [K_b]\{Y_b\} = \{F_b\} \tag{30}$$

where $[M_b]$, $[C_b]$, and $[K_b]$ = vehicle mass, damping, and stiffness matrices, respectively; $\{Y_b\}$ = vehicle displacement vector; and $\{F_b\}$ = vector of the wheel–road contact forces.

In this study, a simply supported girder bridge with two lanes is established by means of grillage method in the software ANSYS, with a span of 30 m and a width of 12 m, as shown in Fig. 9(a). In this model bridge, five identical T-beam girders are arranged under the bridge deck along the width of the bridge, which has a bending stiffness of 1.08×10^{10} N·m^2 and a linear density of 1.87×10^3 kg/m. Rectangle section and T-shape section diaphragms have a spacing of 6 m in the longitudinal direction, with a bending stiffness of 2.90×10^5 and 5.10×10^9 N·m^2, respectively. The Rayleigh damping ratio with a coefficient of $\alpha = 1.76$ and $\beta = 1.20 \times 10^{-3}$ is adopted to calculate the bridge dynamic response.

As shown in Fig. 9(b), a two-axle vehicle, represented by a combination of rigid bodies connected by springs and damping devices, was adopted in the numerical simulations, where M denotes the vehicle weight, m_1 and m_2 denote the weight of the front and the rear axles, k_{s1} and k_{s2} denote the suspension stiffness, k_{t1} and k_{t2} denote the tire stiffness, c_{s1} and c_{s2} denote the suspension damping, c_{t1} and c_{t2} denote the tire damping, I_α denotes moment of inertia, and D_i denotes the axle spacing.

In a vehicle–bridge coupling simulation, the point-contact is taken as the wheel–bridge contact condition. Meanwhile, the road surface condition is set as *Class B* grade (ISO 2016). Road roughness is generally simulated as a zero-mean Gaussian random process in numerical simulation, which can be generated by the inverse Fourier transform of the power spectral density function, as

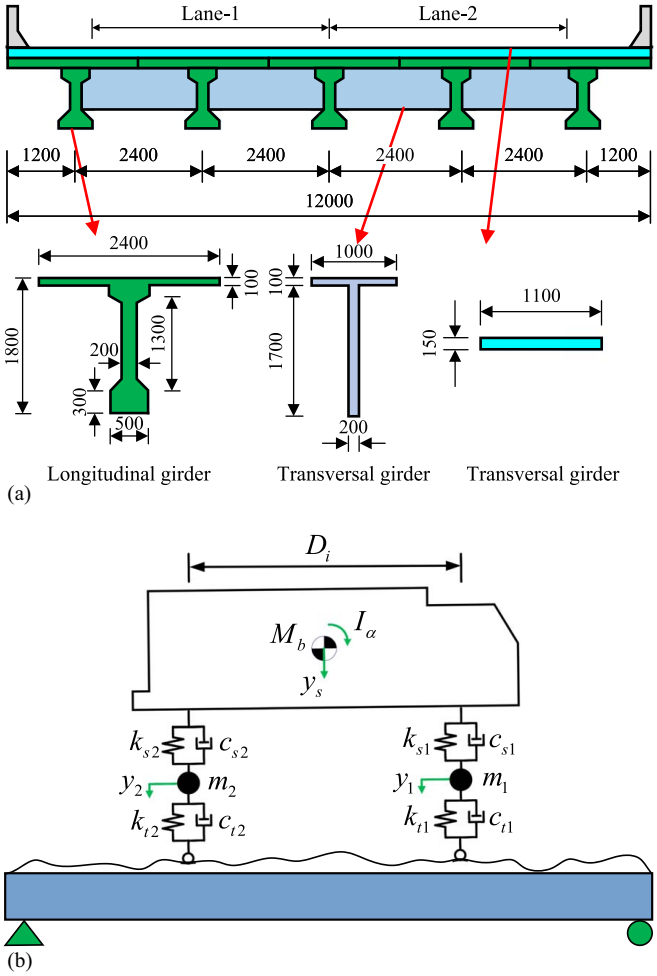

Fig. 9. Bridge and vehicle models: (a) cross section of the bridge (unit: mm); and (b) numerical model of the vehicle system.

follows:

$$r(e) = \sum_{h=1}^{H} \sqrt{2G_q(\Omega_h)\Delta_\Omega}\cos(2\pi\Omega_h e + \beta_h) \tag{31}$$

where $r(e)$ = road roughness at the coordinate of e; β_h = random phase angle uniformly distributed between $0 \sim 2\pi$; Δ_Ω and H = discrete sampling interval and sampling number of spatial frequency, respectively; Ω_h = spatial frequency; and $G_q(\cdot)$ = power spectral density function.

In the computation process, the matrix equation of the vehicle subsystem was calculated by MATLAB program. The vehicle–bridge interaction force was used for the bridge subsystem by introducing ANSYS. The dynamic displacement responses of the bridge were ultimately extracted.

Simulation Setup

A coach truck was adopted to simulate passing over the model bridge alone with randomly generated virtual axle loads. The corresponding vehicle parameters, such as front- and rear-axle weights, suspension damping, tire damping, suspension stiffness, and tire stiffness, were defined with selected values, as shown in Table 2 (OBrien et al. 2010; Deng et al. 2018). It is recommended to run as many loading cases as possible, with 30 being the minimum number of cases.

Table 2. Major parameters of the numerical vehicle model

Vehicle types	m_1, m_2 (kg)	k_{t1}, k_{t2} (kN/m)	k_{s1}, k_{s2} (kN/m)	c_{t1}, c_{t2} (kN·s/m)	c_{s1}, c_{s2} (kN·s/m)
Coach truck	600, 600	1,500, 1,800	400, 400	3, 3	15, 20

Table 3. Random parameter distribution of vehicle numerical model

Vehicle types	a_1	M (kg)
Coach truck	N(0.3580, 0.0252)	U(6000, 18000)

Meanwhile, based on the vehicle data and information base (Zhou et al. 2020), uncertain parameters, such as vehicle weight (M), are randomly generated by uniform distribution [U (min., max.)]. The distribution coefficient of the front-axle weight (a_1) follows a normal distribution [N (mean, variance)] according to the statistical results; hence, the distribution coefficient of the front-axle weight (a_1) is generated randomly according to the normal distribution. Virtual axle load (W_i^r) is the product of vehicle overall weight (M) and axle load distribution coefficient (a_i). M and a_i are generated based on the statistical information of vehicle model as shown in Table 3.

Identification Result

Six hundred groups of virtual axle weights are randomly generated for the Coach truck, in which the motion speed of the Coach truck is 10 m/s and the axle spacing was 5.5 m. Furthermore, the corresponding dynamic displacement response is obtained according to the vehicle–bridge coupling system. In the vehicle–bridge coupling system, the sampling frequency of the vertical displacement of the bridge midspan is set as 100 Hz. According to the Eqs. (9) and (12), it is known that the ordinate vector I of the IL to be estimated contains 300 parameters, namely, $I=[I_1, I_2, \ldots, I_{300}]^T$. The dynamic response and the virtual axle weight are then put into the Bayesian model proposed in the Section "Identification of Influence Lines (Module 4)" to obtain the maximum a posteriori influence line (MAPIL) and posterior probability distribution of the IL. Meanwhile, a realistic IL could be obtained by static loading of the vehicle–bridge coupling system.

The posterior distribution of the IL ordinate can be intuitively illustrated at each sampling point in Fig. 10, which reflects the changes of the IL ordinate along the length of the bridge. The width of the strip curve is positively correlated with the standard deviation of the IL posterior distribution. The dynamic effect makes some parts of the realistic IL locate outside of the 95% confidence interval and makes the identified IL show some fluctuation. The identification error is 5.25% according to the following equation:

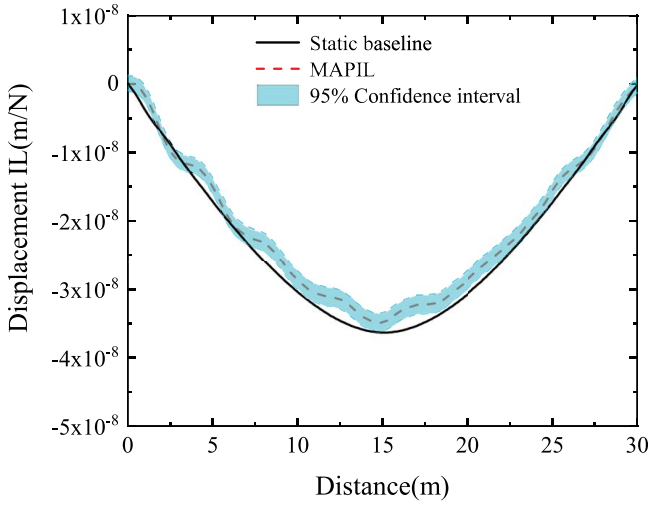

Fig. 10. Results of displacement IL posterior distribution and MAPIL.

$$I_{\mathrm{Err}}=\frac{\sum_{i=1}^{N_a}|I_i^{\mathrm{sta}}-I_i^{\mathrm{MAP}}|}{\sum_{i=1}^{N_a}|I_i^{\mathrm{sta}}|}\times 100\% \tag{32}$$

where I_{Err} = percentage error between the MAPIL and realistic IL; I_i^{sta} and I_i^{MAP} = ith ordinate values of realistic IL and MAPIL, respectively; and N_a = length of the bridge IL vector.

Parametric Study

Calculation of Condition Number

To explore the influence of the condition number of the bridge displacement response on the identification results, the inversion of the posterior distribution of the IL for the Coach truck with 50, 100, 300, and 600 groups of conditions are conducted, and the influence of condition number on the MAPIL identification results evaluated. The motion speed of the Coach truck is 10 m/s and the axle spacing is 5.5 m. The identification error of the MAPIL gradually decreases with the increase of condition number, as shown in Table 4. Furthermore, as shown in Fig. 11, the posterior distribution range of the IL gradually narrows with the increase of the condition number. From the foregoing, it can reasonably be inferred that the accuracy of the MAPIL can be effectively improved by sufficient observed data.

Driving Speed

To study the identification accuracy of the MAPIL at different moving speeds of the vehicle, 600 groups of random conditions are generated at each speed (10, 15, 20, 25, and 30 m/s) for the Coach truck (axle spacing = 5.5 m). A comparison of MAPIL under different speeds is shown in Fig. 12. When the vehicle speed is 10–30 m/s, the identification error relative to the static IL is 5.85%, 6.80%, 7.92%, 9.51%, and 12.13%, respectively. The increase in motion speed causes the dynamic response of the vehicle–bridge coupled system to be enhanced. Furthermore, the amplitude of a bridge's response is enhanced as the speed of the vehicle increases, while the coupling condition between the vehicle and bridge decreases, thereby leading to a decrease in the identification accuracy of the MAPIL with the increase in vehicle motion speed (Zhou et al. 2019, 2021b).

Table 4. Identification errors of MAPIL under different condition numbers

Condition number	I_{Err} (%)
50	10.31
100	10.67
300	7.79
600	5.25

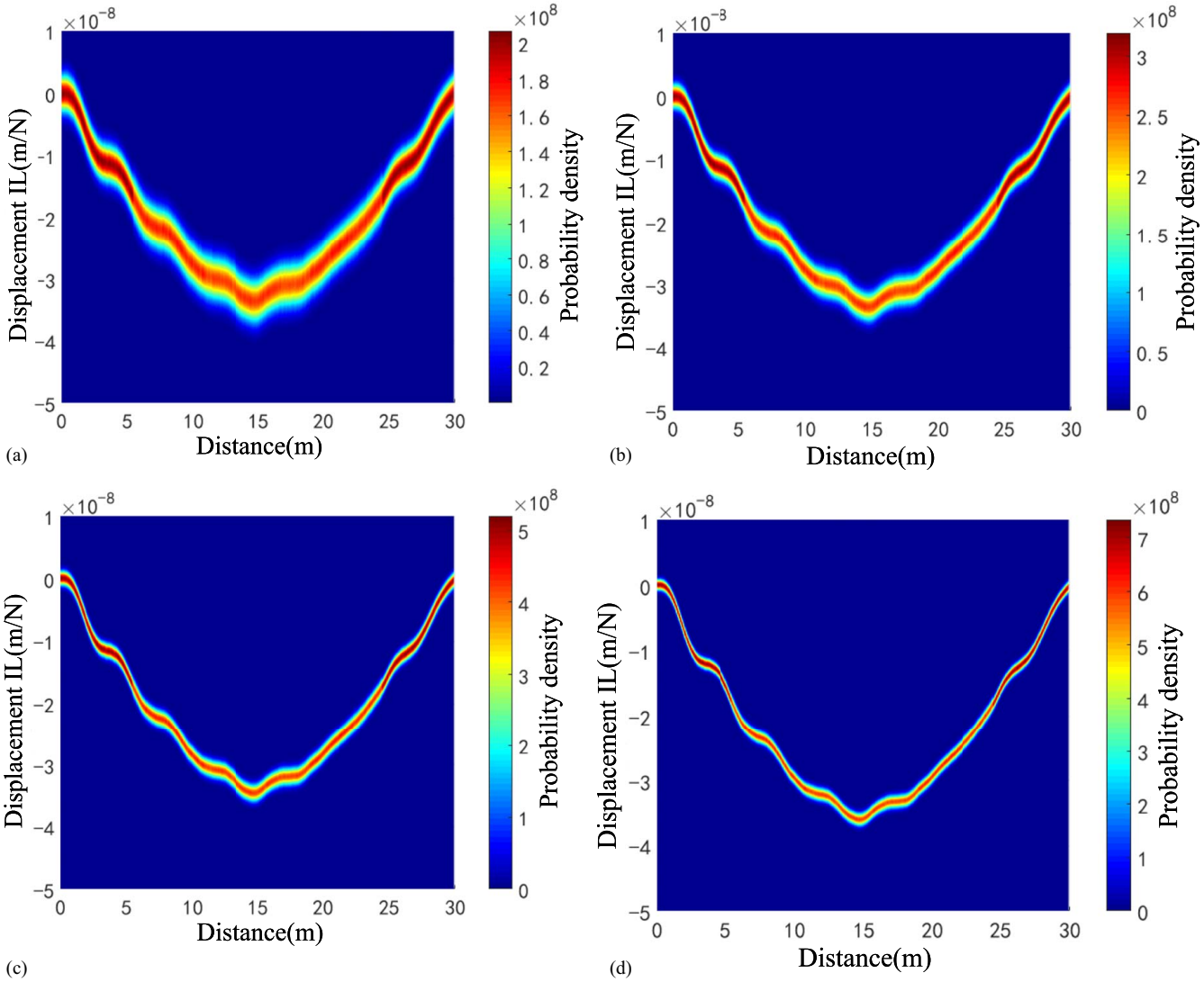

Fig. 11. IL posterior distribution under different condition numbers: (a) 50; (b) 100; (c) 300; and (d) 600.

Laboratory Tests

Experimental Setup

To investigate the accuracy of the IL identification model based on Bayesian Theory (Module 4), experimental tests in a laboratory were conducted. The vehicle–bridge coupled model is composed of an acceleration ramp, a deceleration ramp, a bridge model, and a vehicle model. The lengths of the acceleration ramp and deceleration ramp are 3.0 and 3.1 m, respectively, and both ramps are 2.0 m in height. A horizontal section 1.5 m long is set at the front end of the acceleration ramp to ensure that the passing vehicle travels at a uniform speed. The bridge model is a simply supported multigirder bridge manufactured from polymethyl methacrylate with a scale ratio of 1:0.119, a Young' s modulus of 2,795 MPa, a density of 1,181.6 kg/m^3, a length of 2.38 m, and width of 1.01 m (He et al. 2017). The vehicle model was hauled to a certain height and then released from the acceleration ramp. It gains a certain speed before entering the bridge model, which can be changed by adjusting the original position of the vehicle on the ramp, as shown in Fig. 13(a). A three-axle truck, comprising two vehicle bodies connected by a hinge, is adopted in this study. It has a total length of 1.36 m and a width of 0.2 m. The space between Axle A_1 and Axle A_2 is 0.31 m. The space between Axle A_2 and Axle A_3 is 0.55 m. The load of Axles A_1, A_2, and A_3 are W_1, W_2, and W_3, respectively, as shown in Fig. 13(b). The axle load can be adjusted by adding/removing steel plates.

Six measured points were set at the bottom and deck of the bridge. Since the length of the model bridge is only 2.38 m, the vehicle model passes through the model bridge in a short time (≤2 s) at the research speed ($v_1 = 1.175$ m/s, $v_2 = 1.902$ m/s, and $v_3 = 2.987$ m/s), and the maximum sampling frequency of the VDS under actual field conditions is 30 Hz. Therefore, to obtain a more abundant dynamic displacement response of the bridge and to consider the Nyquist–Shannon sampling theorem comprehensively, one laser displacement meter with the accuracy of 5 μm and the sampling frequency of 1 kHz was employed to obtain the vertical displacement response at the midspan, and three strain gauges were installed under Girder 2. Two resistive strain gauges were installed at the entrance and exit of the bridge to determine the motion speed of the vehicle. The layouts of test points are shown as Fig. 13(c).

The statistical information of axle load distribution coefficient is obtained by adjusting the amount or position of steel plates on the vehicle model. The distribution ranges (min., max.) of the axle load distribution coefficients for a_1_a_3 were (0.12, 0.38), (0.22, 0.46),

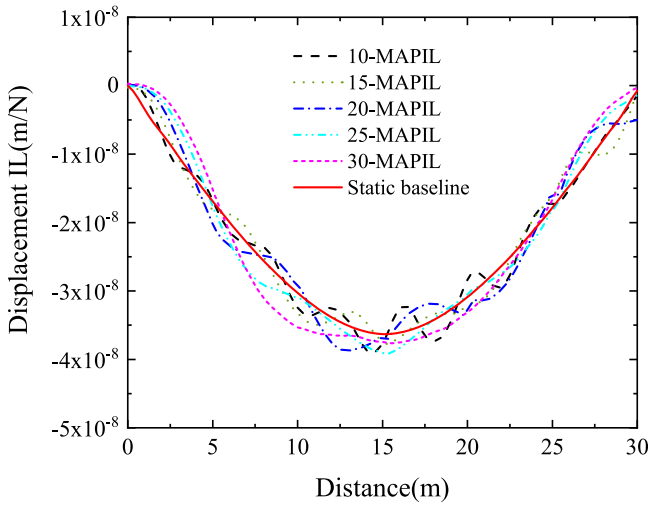

Fig. 12. MAPIL identification results under different driving speeds.

Table 5. Axle-load coefficient of vehicle model

a_1	a_2	a_3	M (kg)
N(0.2366, 0.0589)	N(0.3678, 0.0615)	N(0.3955, 0.0500)	U(23, 42)

and (0.26, 0.52), respectively, which are assumed to be a truncated normal distribution (the mean and variance as shown in Table 5). The model vehicle's motion speed can be adjusted by changing the release position at different heights on the acceleration ramp. Since the driving speed is affected by the friction force of the bridge deck and the rail, the average speed of the vehicle is used to calculate the real-time position of the axle. Furthermore, three motion speeds ($v_1 = 1.175$ m/s, $v_2 = 1.902$ m/s, and $v_3 = 2.987$ m/s) under each loading case are considered, and the drop heights of the front wheels of the model vehicle from the horizontal section corresponding to the three motion speeds are 0.053, 0.121, and 0.351 m, respectively. The foregoing motion speeds are equal to 10–32 km/h for an actual full-scale vehicle.

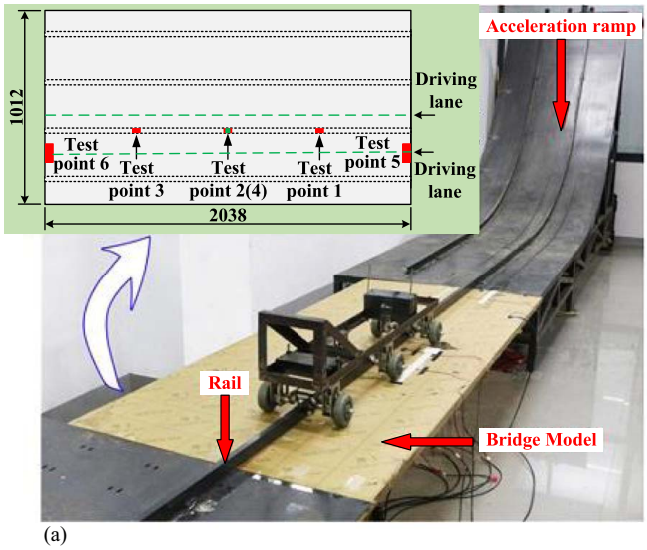

(a)

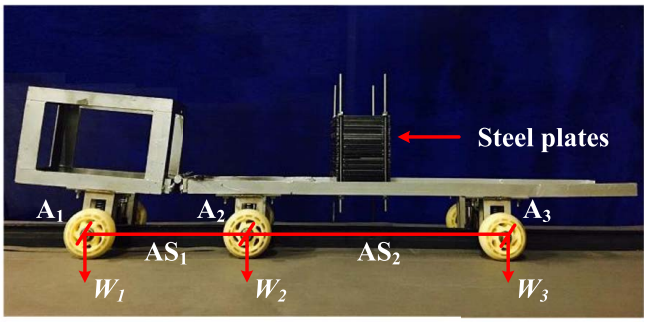

(b)

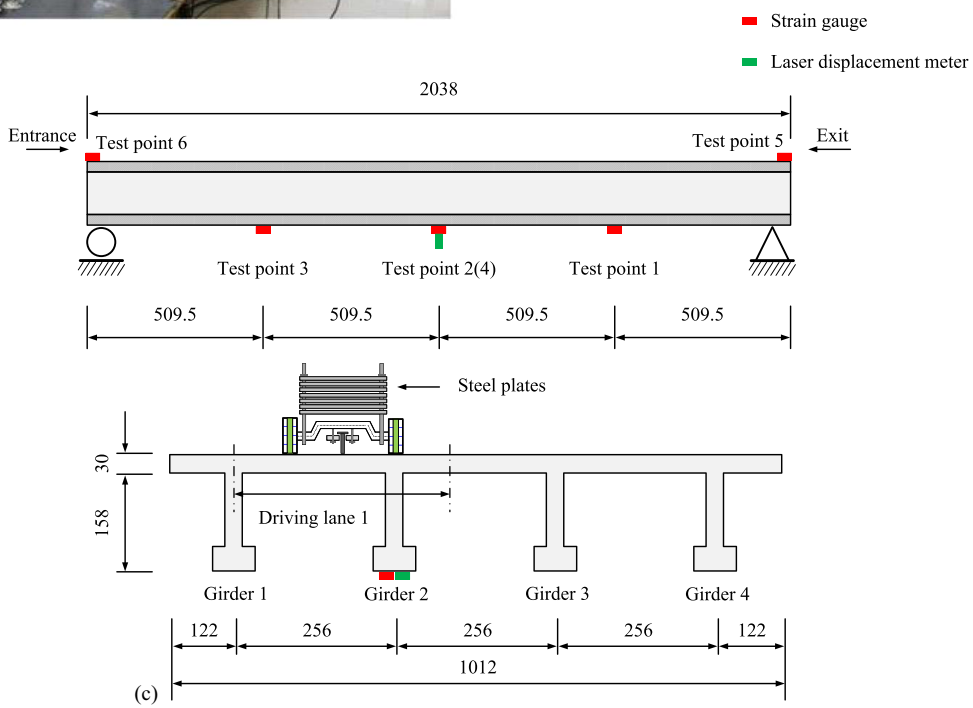

(c)

Fig. 13. Experimental setup: (a) test platform; (b) scaled three-axle vehicle model; and (c) sensor positions (unit: mm).

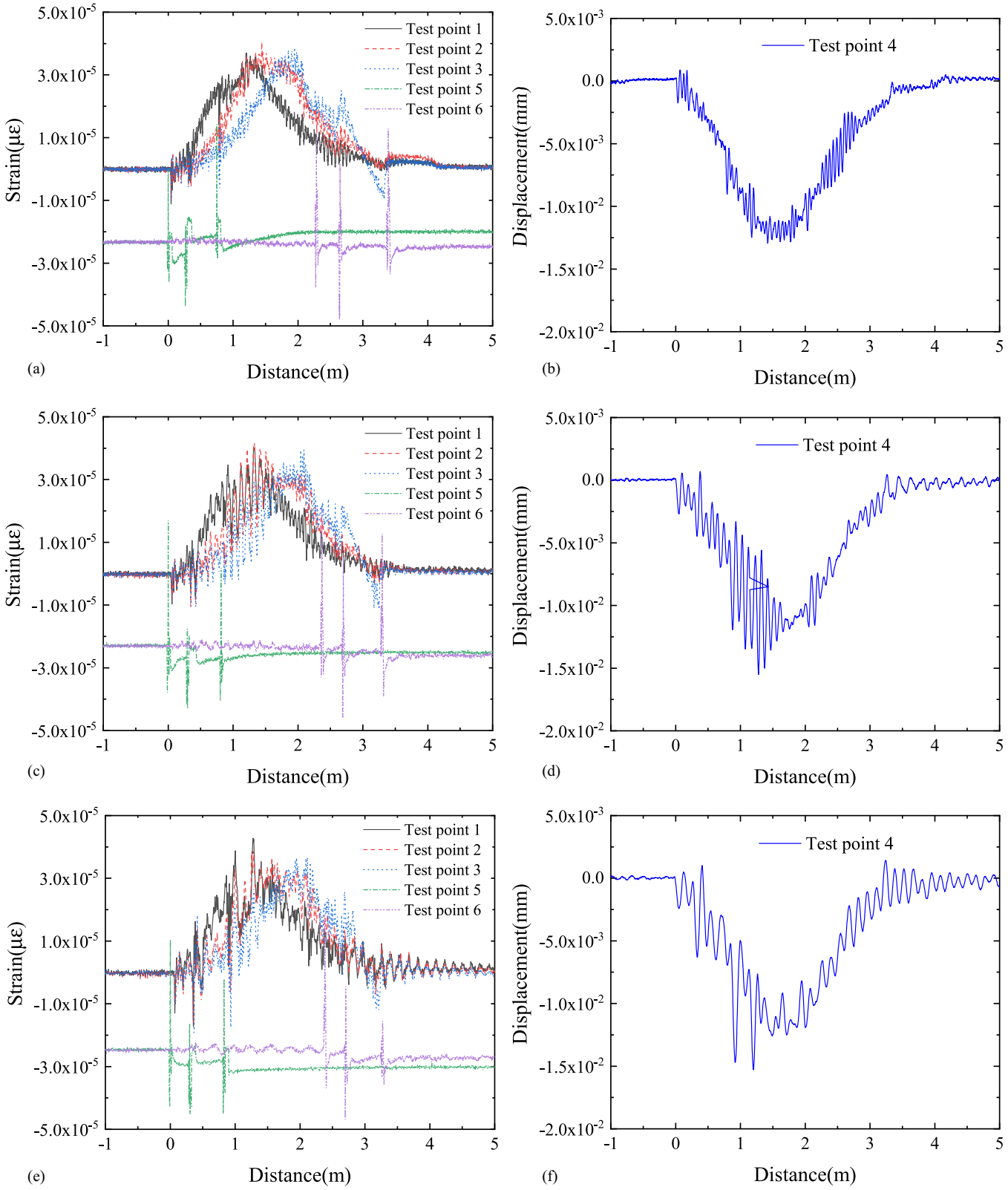

Fig. 14. Measured strains and displacements: (a) v_1-strain; (b) v_1-displacement; (c) v_2-strain; (d) v_2-displacement; (e) v_3-strain; and (f) v_3-displacement.

Bridge Responses Analysis

The vehicle motion speed is adjustable to within 1.175–2.987 m/s. By adding/removing steel plates [shown in Fig. 13(b)], as many loading cases as possible are increased in diversity, and 200 loading cases (M1–M200, loads up to 41.219 kg, approximately 0.66 kg per loading case) were designed by changing the vehicle from an unloaded state to a fully loaded state. Take the loading case of M1 ($W_1 =$ 5.7 kg, $W_2 = 11.3$ kg, and $W_3 = 11.145$ kg) as an example. Three vehicle motion speeds ($v_1 = 1.175$ m/s, $v_2 = 1.902$ m/s, and

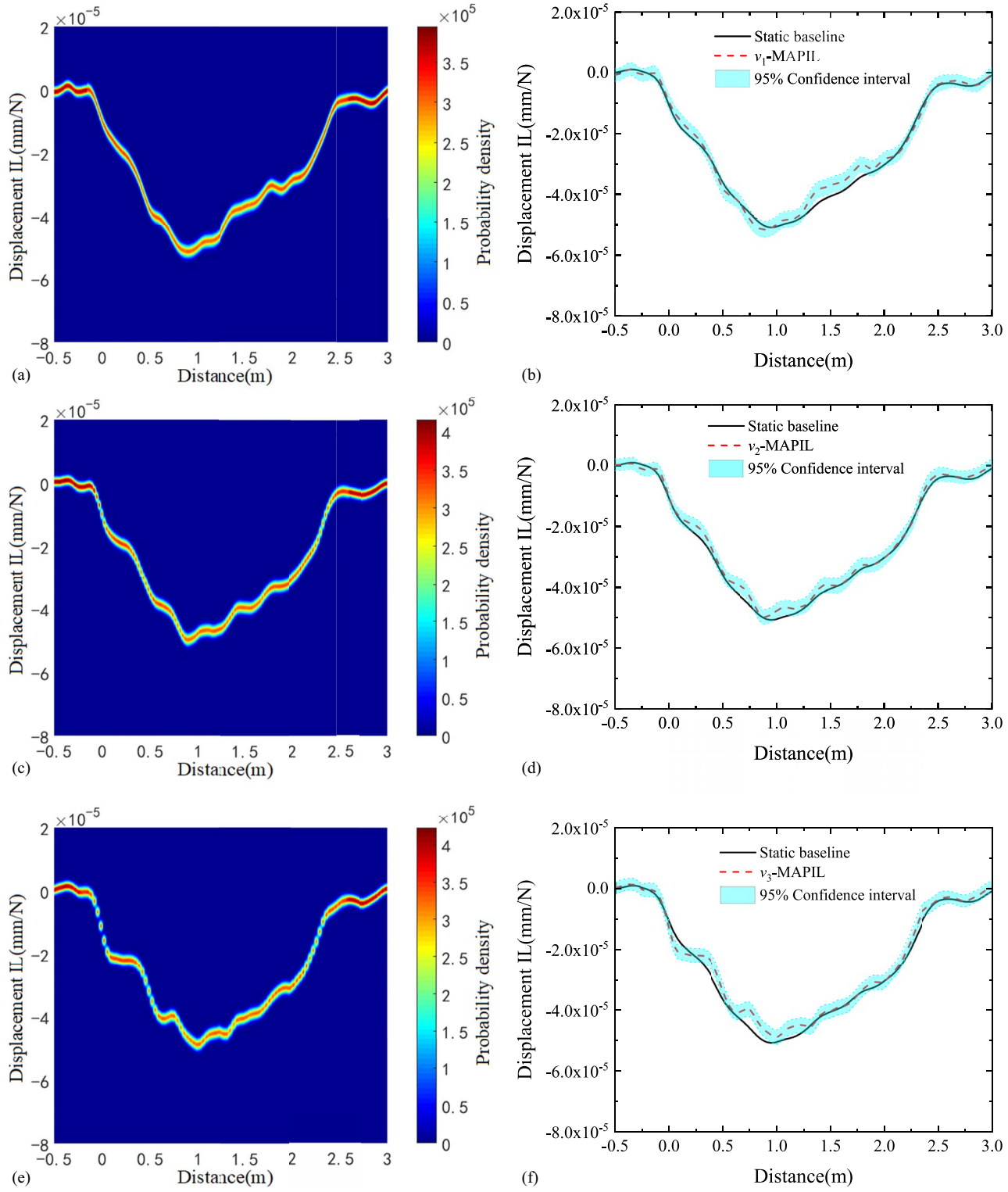

Fig. 15. Results of displacement IL posterior distribution and MAPIL under different motion speeds: (a) posterior distribution of IL under v_1 condition; (b) MAPIL under v_1 condition; (c) posterior distribution of IL under v_2 condition; (d) MAPIL under v_2 condition; (e) posterior distribution of IL under v_3; and (f) MAPIL under v_3 condition.

$v_3 = 2.987$ m/s) were investigated for each loading case to increase the diversity of the test samples. The speed of the vehicle can be identified from the signals measured from Test points 5 and 6. The sampling frequency of the test points is 1 kHz to obtain a detailed IL. The collection results are plotted in Fig. 14. The local vibrations related to the motion speed of vehicles can be observed, which appear on the measured signals due to wheel–deck interaction.

Identification Result

The dynamic response of displacement and strain can be measured by Test points 2 and 4, respectively. The axle load distribution coefficients follow the normal distribution [N (mean, variance)] according to the statistical results of the vehicle model, and then the axle load distribution coefficients are randomly generated

Table 6. Estimation results of I_{mid} under different motion speeds

Condition	MAP (mm/N)	True value (mm/N)	Standard deviation	95% confidence interval (mm/N)	Error I_{Err} (%)
v_1	-4.685×10^{-5}	-4.72×10^{-5}	1.29×10^{-6}	$[-4.431 \times 10^{-5}, -4.945 \times 10^{-5}]$	0.74
v_2	-4.578×10^{-5}	-4.72×10^{-5}	1.23×10^{-6}	$[-4.331 \times 10^{-5}, -4.579 \times 10^{-5}]$	3.00
v_3	-4.532×10^{-5}	-4.72×10^{-5}	1.22×10^{-6}	$[-4.295 \times 10^{-5}, -4.780 \times 10^{-5}]$	3.98

according to the normal distribution. To ensure the uncertainty of the virtual axle weight, the vehicle overall weight (M) is generated randomly according to a uniform distribution [U (min., max.)] based on the statistically obtained distribution interval (min. = 23 kg, max. = 42 kg). Virtual axle load (W_i^r) is the product of vehicle overall weight (M) and axle load distribution coefficient (a_i). M and a_i were generated based on the statistical information of the vehicle model as shown in Table 5. The dynamic response and the virtual axle weight were then put into the Bayesian model proposed in Section "Identification of Influence Lines (Module 4)" to obtain the MAPIL and posterior probability distribution of the IL. Meanwhile, a realistic IL could be inversely calculated through Eq. (10) or Eq. (11), based on the vehicle weighing results and corresponding measured responses.

The posterior distribution of the displacement IL under different motion speeds is obtained by Bayesian inversion calculation of the IL parameters in the full-length range of the bridge model, as shown in Figs. 15(a, c, and e). With the increase of driving speed, the probability density corresponding to the MAPIL decreased significantly, and the identification results of the IL ordinate indicate greater uncertainty. As shown in Figs. 15(b, d, and f), the identification results of MAPIL are compared with the static displacement IL. The identification errors are 3.09%, 4.17%, and 4.88%, respectively. Therefore, the error of MAPIL identification results increases with the increase in speed. The reason for this is that the dynamic response of the coupled vehicle–bridge system increases as the speed of motion increases, which causes the amplitude of the bridge response to enhance and move more and more away from the static baseline.

In real life, an increase of 10 km/h in vehicle driving speed will increase the identification error of MAPIL by almost 1%. Furthermore, in real life, when the vehicle is traveling at a speed of 1 m/s, the identification errors of IL obtained by least square method for time domain model (LS), regularized fast Fourier

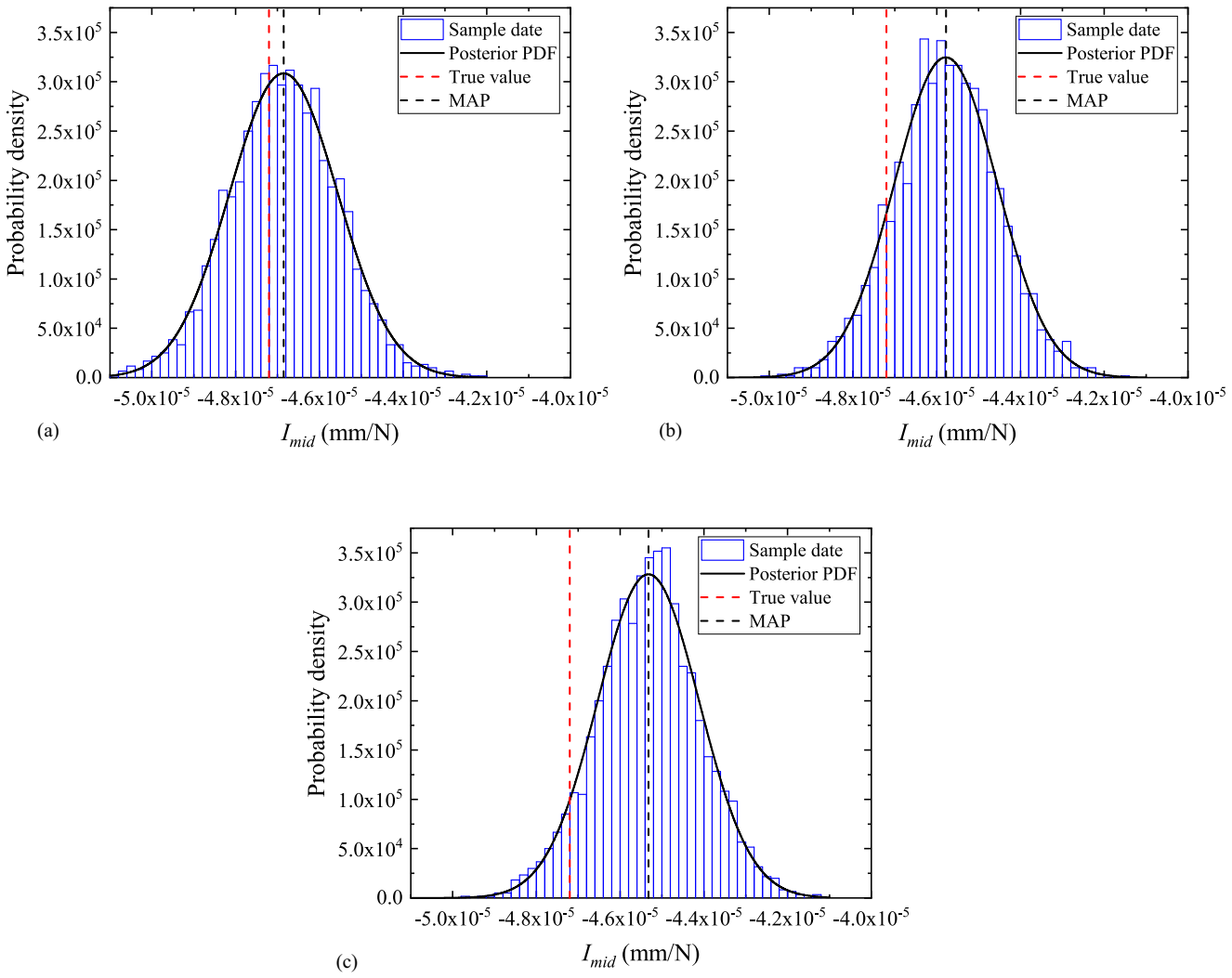

Fig. 16. Posterior distribution of samples under different motion speeds: (a) v_1; (b) v_2; and (c) v_3.

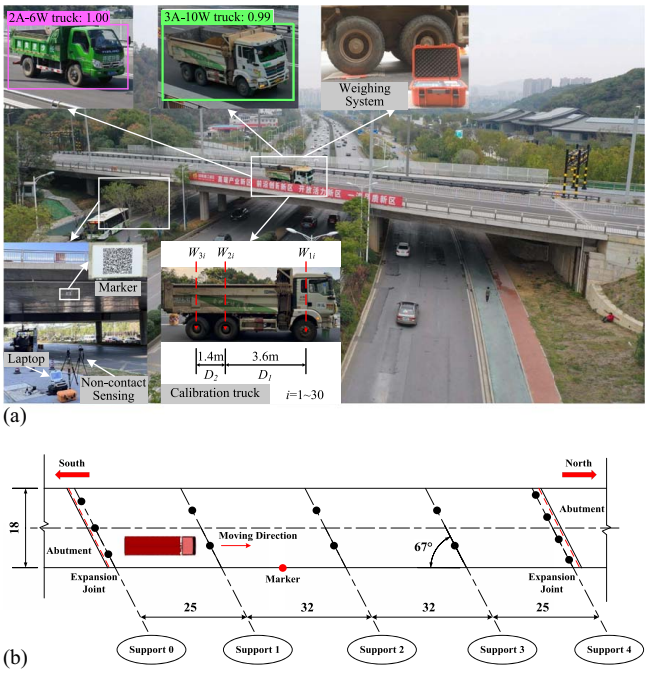

Fig. 17. (a) Panoramic view of the bridge; and (b) vertical view and truck routines (unit: m).

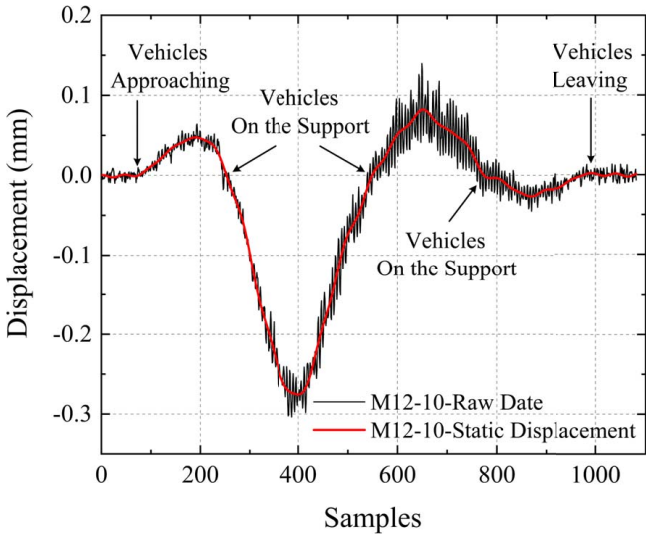

Fig. 18. Raw data and extracted static data at the midspan of the bridge.

transformation method for frequency domain (FD), and Tikhonov regularization method for time domain model (L2R) were 5.5%, 16.5%, and 3.6%, respectively. Therefore, an increase in speed of 1 m/s with a decrease in accuracy of 1% is acceptable (Zheng et al. 2019a). Additionally, under different driving speed conditions (v_1, v_2, and v_3), the MAP of parameter I_{mid} approaches the ordinate value of the displacement IL. The estimation results of the parameter I_{mid} are presented in Table 6 and the posterior distribution of samples is shown in Fig. 16.

Field Tests

Rapid Bridge IL Identification Test Setup

To verify the effectiveness and robustness of the proposed method, a field test was conducted on a four-span continuous box-girder bridge in Changsha, China. The main span layout of the bridge is 25 m + 32 m + 32 m + 25 m, with basin-type rubber supports, cast-in-place concrete box girders, reinforced concrete piers, and pile foundations. The bridge employs seat abutments and column bents with deep foundations, as shown in Fig. 17.

The bridge has four traffic lanes. The field test focused on the vertical displacement of the measurement point in the midspan of the bridge. A VDS was fixed on the southeast bank of the bridge for stationary noncontact sensing by attaching a 250 mm × 250 mm marker in the midspan. Under the field test conditions, the sampling frequency was chosen as high as possible and the Nyquist–Shannon sampling theorem was considered comprehensively to obtain a more abundant dynamic displacement response of the bridge to get a detailed IL. The sampling rate of the system was set as 30 Hz, and measuring precision was 0.001 mm. The VDS is equipped with a black-and-white array camera for measurement with a resolution of 1,920 × 1,200 pixels and a focal length of 100–400 mm.

A 3A–10W calibration truck, shown in Fig. 17(a), was prepared for the moving test at the speeds of 10–30 km/h. By changing the vehicle load, as many loading cases as possible were run within the given time frame for testing, which ultimately ended up being 30 tests. Thirty loading cases (M1–M30, loads up to 24,540 kg, approximately 400 kg per loading case) were designed by changing the vehicle from empty state to a fully loaded state. To ensure the accuracy of MAPIL identification results, it is recommended that the loading cases should be no lower than 30. Furthermore, three motion speeds (10, 20, and 30 km/h) were designed for each loading case. For each test, the vehicles were driven over the bridge from one end to the other end, as shown in Fig. 17(b).

Because only static responses are of interest for IL identification, the FFT low pass filter (frequency-domain method) (Brigham 1988; Moon and Choi 2000) is used to discard the dynamic part of the raw data while keeping the static responses (Khuc and Catbas 2018). The natural frequency of the bridge is 5.18 Hz, which can be regarded as a cutoff frequency of dynamic fluctuation elimination (Zheng et al. 2022). The comparison of the raw data with the static displacements for a vehicle loading case of M12 and a vehicle motion speed state of 10 km/h is shown in Fig. 18. The corresponding realistic IL for each condition can be obtained by Eq. (8) or Eq. (9) based on the static responses of the bridge midspan measurement point for 3A–10W truck under different axle loads (preknown) and vehicle motion speed states. Then, the static baseline IL can be obtained by calculating the mean results of IL for a

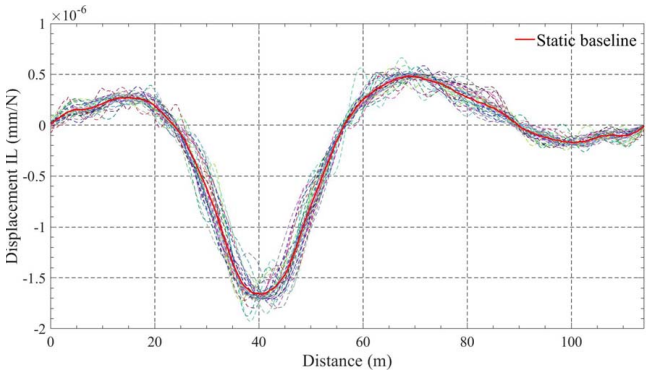

Fig. 19. The static IL at midspan of the bridge.

Table 7. Virtual axis weight matrix parameters of a 3A–10W truck

D_1 (mm)	D_2 (mm)	W_1^r (kg)	W_2^r (kg)	W_3^r (kg)
3,600	1,400	N(4,695.43, 1,389.83)	N(5,880.83, 1,720.50)	N(5,880.83, 1,720.50)

3A–10W truck under 3 vehicle motion speeds and 30 loading conditions, as shown in Fig. 19.

The midspan displacement responses of the bridge caused by a 2A–6W truck in random traffic flow passing alone over the bridge were collected, as many as possible within the given time frame, with a total of 56 records ultimately obtained to ensure the accuracy of MAPIL identification. The midspan displacement response of the bridge is 0 when the truck passes over the bridge piers, and the motion speed of the truck passing over each span of the bridge is determined based on the time difference and distance between the truck passing through the adjacent piers.

Video Identification and Vehicle Information Prediction

An UAV was used to obtain the vehicle image information on the test bridge, and the vehicle identification and classification algorithm proposed in the Section "Identification of Vehicle Types (Module 1)" was used to identify the vehicle type of vehicles passing over the bridge with more than a 99% accuracy.

The distribution intervals of the uncertain parameters of axle spacing, overall weight, and axle load distribution coefficient of the identified vehicle types were defined according to the vehicle data and an information base established. For a 3A–10W truck, the overall weight was obtained by uniform random sampling in the overall weight interval, and the virtual axle load (W_1^r, W_2^r, and W_3^r) of each axle was obtained according to the established vehicle data set [Section "Estimation of Vehicle Loads (Module 2)"] under the premise of satisfying the distribution interval of axle load distribution coefficient. Then, the virtual axle load distribution of each axle was obtained, and the axle spacing was obtained by measurement, as shown in Table 7, where the virtual axle load (W_i^r) of each axle is equal to the overall weight multiplied by the axle load distribution coefficient of its corresponding axle.

For a 2A–6W truck, the distribution of virtual axle load (W_i^r) of each axle was obtained by the same method, but the difference was that the distribution of axle spacing was obtained according to the vehicle data and information base established, and the axle spacings were obtained by uniform random sampling from the distribution of axle spacing, as shown in Table 8. Therefore, the virtual matrix of axle load was obtained by virtual axle load and axle spacing.

Identification Results

The measured static responses and the virtual axle weight matrix parameters were then put into the Bayesian model proposed in Section "Identification of Influence Lines (Module 4)" to obtain the MAPIL and posterior probability distribution of the IL. The posterior distribution of the displacement IL for a 3A–10W truck and a 2A–6W truck under variable motion speeds (speed varies between 10–30 km/h at moment to moment) were obtained by Bayesian inversion calculation of the IL parameters in the full-length range of the bridge model, as shown in Fig. 20.

Table 8. Virtual axis weight matrix parameters of a 2A–6W truck

D (mm)	W_1^r (kg)	W_2^r (kg)
N(3,489.46, 669.34)	N(4,270.86, 1,362.50)	N(6,565.57, 2,335.93)

The posterior distribution of displacement IL of a 2A–6W truck has a wider range than that of a 3A–10W truck, meaning that the variance of the ordinate posterior distribution is large. This is mainly because the axle weight of 3A–10W trucks was obtained from the vehicle database in constructing the virtual axle weight matrix, while their axle spacing was measured. However, the axle weight and axle spacing of 2A–6W trucks were obtained from the vehicle database. In addition, the overall weight of a 2A–6W truck is smaller than that of a 3A–10W truck, so a 2A–6W truck produces less excitation response to the bridge, which makes the dynamic disturbance in the collected dynamic displacement response have more influence on the static response in the raw data, increasing the midspan displacement response error of a 2A–6W truck. Hence, the posterior distribution presents greater uncertainty.

Fig. 21(a) compares the identification results of MAPIL for a 3A–10W truck under different speeds (10, 20, and 30 km/h) with the static baseline displacement. The errors are 3.73%, 4.30%, and 4.62%, respectively. Therefore, the error of MAPIL identification results increases with the increase in motion speed. Fig. 21(b) compares the identification results of MAPIL for the 3A–10W truck and the 2A–6W truck under variable speeds (speed varies between 10–30 km/h at moment to moment) with the static baseline displacement. The errors are 3.14% and 11.48%, respectively. The MAPIL results were sharper for the 2A–6W truck with the span where the measurement point of the test bridge was located, indicating that the truck type had a greater influence on the MAPIL identification results.

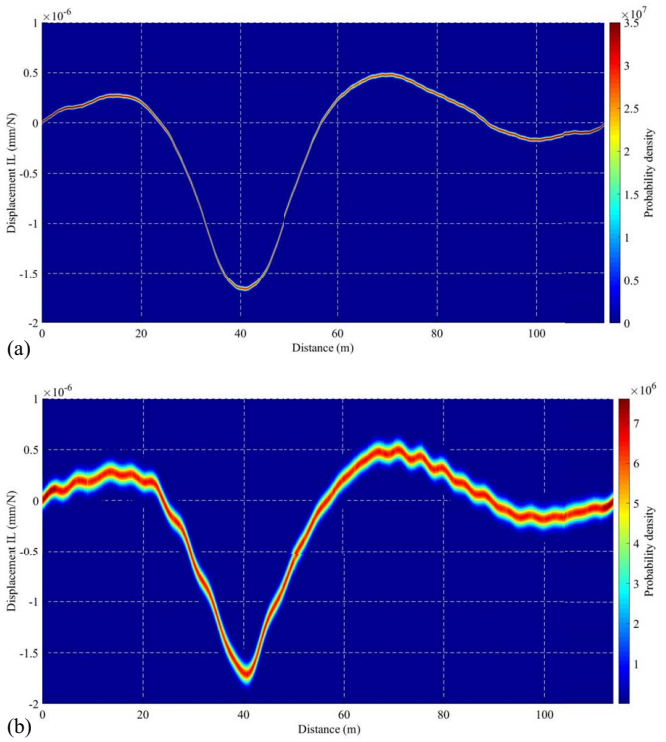

Fig. 20. Identification results of IL posterior distribution under variable motion speeds: (a) 3A–10W truck; and (b) 2A–6W truck.

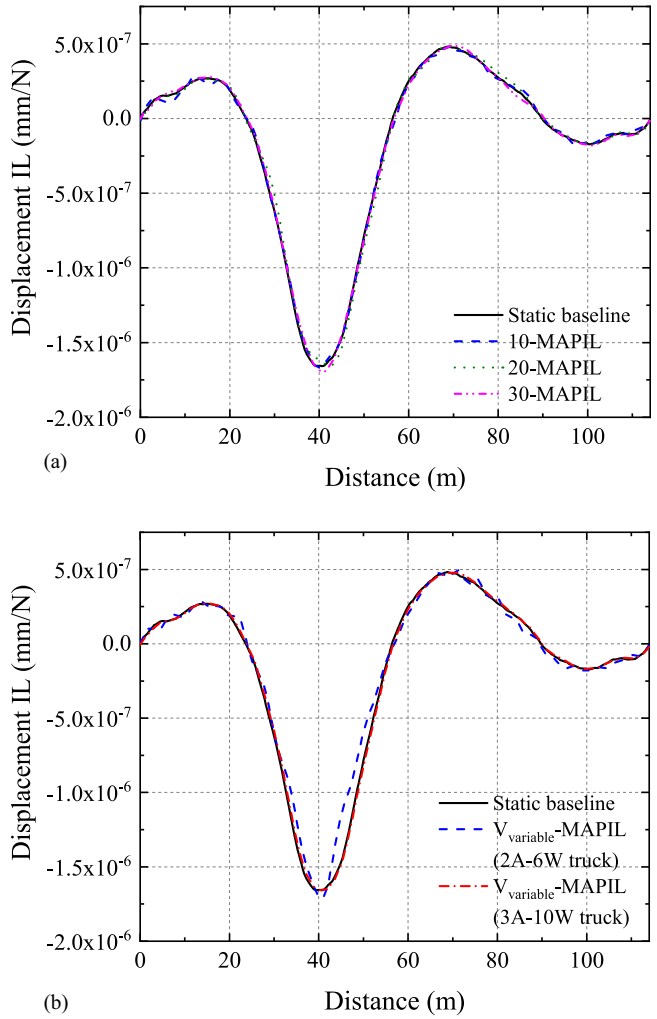

Fig. 21. MAPIL identification results: (a) 3A–10W truck under different motion speeds; and (b) 2A–6W truck and 3A–10W truck under variable motion speeds.

To further evaluate the convenience and accuracy of the proposed method, the results of the proposed algorithm and IL identification algorithm based on AAIL proposed by the authors in previous research (Zhou et al. 2021b) were compared for the IL identification of the bridge midspan measurement points under variable speed motions of the 3A–10W truck.

The process of IL identification algorithm based on AAIL is as follows (Zhou et al. 2021b).

First, obtain the axle weight interval $[\underline{w_i}, \overline{w_i}]$ $(i = 1, \ldots, Q)$ of any axle of the vehicle under all loading conditions, where $\underline{w_i}$ and $\overline{w_i}$ denote the lower and upper bounds of the weights matrix of the ith axle of a Q-axle vehicle, respectively. Representing the axial weight interval variable $[\underline{w_i}, \overline{w_i}]$ as the affine form (Stolfi and De Figueiredo 1997; Moore et al. 2009), we get

$$w_i^{\mathrm{I}} = [\underline{w_i}, \overline{w_i}] = x_{i0} + x_{i1} \times \varepsilon_i \tag{33}$$

where x_{i0} = central value of the affine form w_i^{I}; x_{i1} = partial deviations and is defined as a series of floating-point numbers; and ε_i = noise symbols whose values are unknown but assumed to lie within the interval of $[-1, +1]$. During the computation process, the data set $\{x_{i1}\}$ determines the uncertainty value and $\{\varepsilon_i\}$ offers a possibility to take account and keep track of variable dependency.

Therefore, the matrix $[W]_{K,K-C_Q}$ in Eq. (10) can be simplified as follows:

$$W^I = X_0 + X_1\varepsilon_1 + X_2\varepsilon_2 + \cdots + X_Q\varepsilon_Q \tag{34}$$

Setting $B_i = X_0^{-1}X_i$, $A^I = (L_I + B_1\varepsilon_1 + B_2\varepsilon_2 + \cdots + B_Q\varepsilon_Q)^{-1}$, where L_I is the identity matrix. The upper and lower bounds of this interval matrix can be calculated by applying the Newman expansion to A^1 (Degrauwe et al. 2010), which results in

$$\begin{cases} \bar{A} = L_I + \left|\sum_{i=1}^{Q} B_i\right| + \left|\sum_{i=1}^{Q} B_i\right|^2 \left[L_I - \left|\sum_{i=1}^{Q} B_i\right|\right]^{-1} \\ \underline{A} = L_I - \left|\sum_{i=1}^{Q} B_i\right| + \left|\sum_{i=1}^{Q} B_i\right|^2 \left[L_I + \left|\sum_{i=1}^{Q} B_i\right|\right]^{-1} \end{cases} \tag{35}$$

The upper and lower bounds of the IL can be obtained by combining Eq. (10) as follows:

$$\begin{cases} \{\overline{I^I}\} = \underline{A} X_0^{-1}\{Y^m\} \\ \{\underline{I^I}\} = \bar{A} X_0^{-1}\{Y^m\} \end{cases} \tag{36}$$

Considering a classification problem, the input data set in the support vector machine (SVM) are represented as the vectors $\vec{q}_i \in R^n$ with corresponding labels. Solve for the upper and lower bounds of IL in each case, and the label values "+1" and "−1" are given to the upper and lower bounds of IL, respectively. During the calculation process, given a data set $(\vec{q}_i, la_i)$, $\vec{q}_i \in R^n$, $la_i \in \{-1, +1\}$, $i = 1, \ldots, n$, where $(\vec{q}_i, la_i)$ is labeled as the training data set. Then, the quadratic optimization problem is constructed and solved by the sequential minimal optimization algorithm. The binary classification and primal optimization problem could be stated as follows:

$$\min_{\alpha} \frac{1}{2}\sum_{i=1}^{n}\sum_{i=1}^{n} \alpha_i\alpha_j la_i la_j \phi(q_i \cdot q_j) - \sum_{i=1}^{n} \alpha_i \rightarrow s.t. \begin{cases} \sum \alpha_i la_i = 0 \\ 0 \le \alpha_i \le PF \end{cases}$$

$$(i = 1, \ldots, n) \tag{37}$$

where $\phi(q)$ = a nonlinear function that maps the input data to the feature space; $\alpha_i \ge 0$ and $\alpha_j \ge 0$ = Lagrange multipliers; and PF = penalty parameter of the error term defined by the users.

The optimal decision function can be expressed as follows:

$$f(q) = \mathrm{sign}\left(\sum_{i=1}^{n} \alpha_i^* la_i \kappa(q_i, q) + b^*\right) \tag{38}$$

where κ = SVM kernel function, which could effectively avoid the dimensional catastrophe problem of the algorithm. The radial-based function (RBF) is selected for the SVM classification due to its wide convergence domain and powerful nonlinear mapping capability (Smola and Schölkopf 2004). The RBF can be expressed as follows:

$$\kappa(q_i, q_j) = \exp\left(-\frac{g \cdot |q_i - q_j|^2}{2}\right) \tag{39}$$

A good setting of the parameters PF and g, which is estimated by a grid search method based on cross-validation, and the corresponding model is the final SVM. Input the block grid pixel points into the SVM to obtain decision classification results, and then extract the coordinates of the gradient change to form the approximate IL.

From the statistical results of 30 loading cases, the accurate weight interval of the three axles were obtained as (3,870, 6,720), (4,120, 9,410), and (4,020, 9,510) kg. Using M12 (motion speed of 10 km/h) as an example, the distinguished distribution intervals of the displacement IL are shown in Fig. 22(a). Based on the

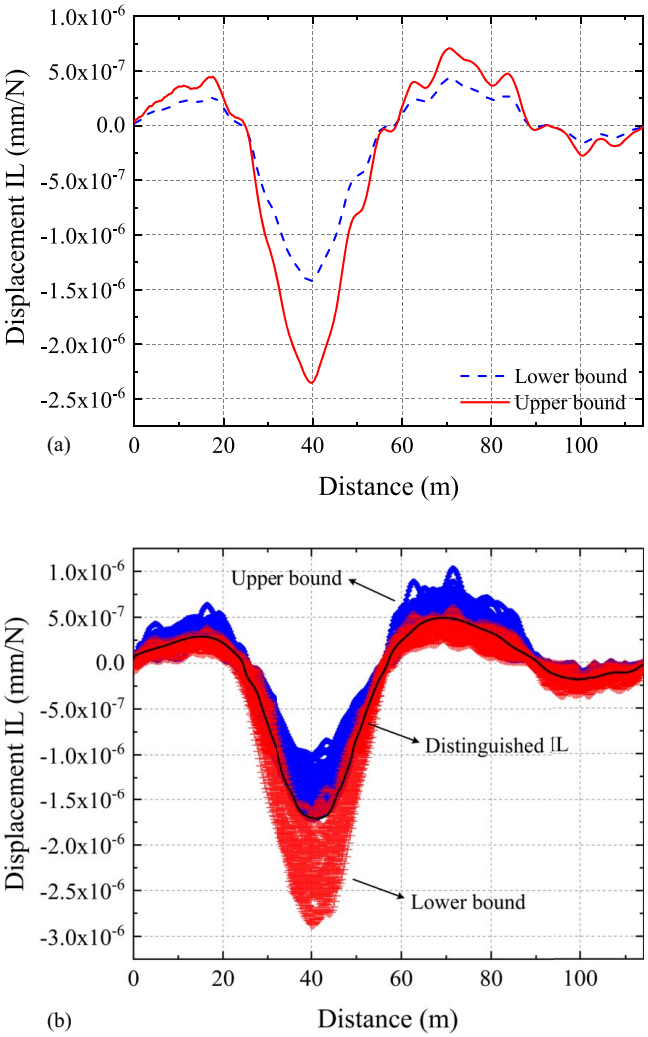

Fig. 22. AAIL identification results: (a) results of upper and lower bound of IL intervals distinguished by AA; and (b) results of displacement IL distinguished by SVM.

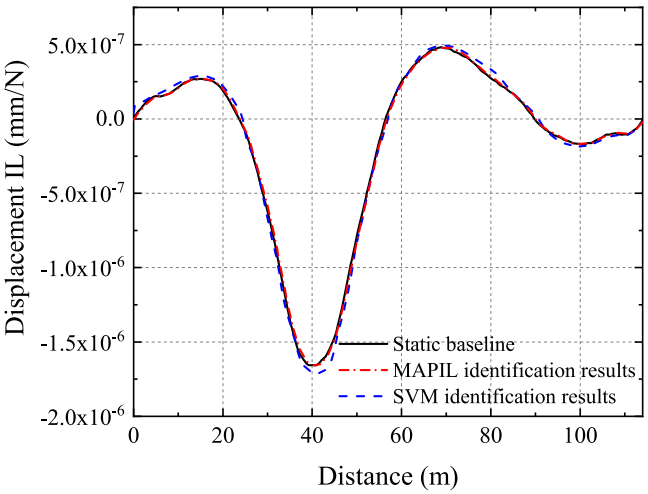

Fig. 23. MAPIL and SVM identification results.

obtained IL intervals of 90 testing cases (three motion speeds for each loading case), the SVM was employed to distinguish the actual IL among the various envelop solutions. Furthermore, various tests were conducted to investigate the identification efficiency under different driving and loading states. The calculated results of displacement IL distinguished by SVM are shown in Fig. 22(b).

As shown in Fig. 23, the MAPIL and SVM identification results of 3A–10W trucks under variable speed motion were compared with the static baseline displacement IL, and the identification errors were 3.14% and 6.99%, respectively. The results showed that the prediction accuracy of both methods was relatively higher. The advantage of the method proposed in this paper is that the displacement IL can be obtained based only on the response of the bridge measurement location combined with the vehicle parameter information obtained from video recognition. The method does not need accurate vehicle axle load intervals and axle spacing, and the accuracy of displacement IL identification is slightly higher.

Conclusions

This paper proposes a noncontact method to identify IL of single-lane highway bridges based on machine vision. The vehicle type was obtained by a YOLO4 network with CBAM. The virtual axle load matrix parameters were obtained based on the vehicle data and information base established. Unit IL decomposition method and Bayesian parameter estimation were utilized to determine the IL. The feasibility and accuracy of the proposed method were investigated through laboratory and field experiments. The conclusions are summarized as follows:

(1) The YOLOv4 network combined with CBAM was able to identify the vehicle types under various traffic flow scenes, illumination conditions, and vehicle speeds. The accuracy was higher than 96%. The identified vehicle type was then used to determine vehicle parameter information according to statistical results of vehicle types and vehicle parameter information.

(2) The IL identification method based on unit IL decomposition and Bayesian parametric estimation has a relatively high accuracy for IL identification. The identification accuracy of displacement MAPIL is lower than 5% according to laboratory experiments. The identification accuracy of displacement MAPIL of the 3A–10W truck is also lower than 5%, according to the field experiments. The MAPIL identification accuracy for the displacement of the 2A–6W truck passing alone over the bridge in stochastic traffic flow is 11.48%. The numerical simulation verifies that the MAPIL identification accuracy increases with the number of conditions. Numerical simulations, laboratory tests, and field experiments have demonstrated that MAPIL identification accuracy decreases with increasing vehicle speed.

(3) Both MAPIL and AAIL control the displacement IL identification error under varying speeds of the 3A–10W truck within an acceptable range, with errors of 3.14% and 6.99%, respectively. Compared with the AAIL method, the method proposed in this paper without having to obtain accurate vehicle axle load interval and axle spacing offers higher accuracy in identifying displacement IL. Future studies can be conducted to enhance the accuracy of the proposed method through finer classification of vehicle types, and the identification of a 2A–6W truck at different speeds.

The method proposed in this paper combines computer vision technology to accomplish IL recognition of single-lane bridges without preknown accurate vehicle axle load intervals and axle spacing. Although the method is currently limited in application to IL identification of single-lane bridges, it shows great potential identifying ILs on multilane bridges. Conversely, the mixed response of multivehicle excited bridges and multilane bridges can

be effectively separated by advanced methods such as the blind source separation algorithm. It is therefore suggested that future related research should focus on IL identification of multivehicle excitation and multilane bridges.

Data Availability Statement

The data that support the findings of this study are available upon request.

Acknowledgments

The authors sincerely appreciate the funding support provided by the National Natural Science Foundation of China (NSFC) (Nos. 51878264 and 52278306), the Science and Technology Progress and Innovation Project of the Department of Transportation of Hunan Province (No. 201912), the Key Research and Development Program of Changsha City (kq1801010), and the Key Research and Development Program of Hunan Province (No. 2022SK2096).

Notation

The following symbols are used in this paper:

AAP = average accuracy of all categories;
A_i = the ith axis;
AP = accuracy of the model in a certain category;
AvgPool = channel-based global average pooling;
a_i = axle load distribution coefficient;
C = model class;
$[C_b]$ = vehicle damping matrix in numerical model;
C_i = sampling point difference between the first axle and the ith axle;
c_{s1}, c_{s2} = suspension damping of the front and the rear axles in numerical model;
c_{t1}, c_{t2} = tire damping of the front and rear axles in numerical model;
D = dynamic data;
D_i = axle spacing;
D_Q = distance from Axle-1 to Axle-Q;
E = number of bridge response conditions included in the calculation;
$E[\cdot]$ = expectation;
F = input feature map;
F' = output feature map of the channel attention module;
F'' = feature map output by the CBAM;
f = sampling frequency;
$f^{7\times7}$ = convolution operation with the filter size of 7×7;
FN = number of positive samples incorrectly predicted;
FP = number of negative samples incorrectly predicted;
$\{F_b\}$ = vector of the wheel–road contact forces in numerical model;
G = number of detected categories;
$G_q(\cdot)$ = power spectral density function;
H = sampling number of spatial frequency;
h = number of parameters;
$I_{(K-C_i)}$ = influence coefficient of the bridge corresponding to the ith axle;
$\{I\}_{K-C_Q,1}$ = vector consisting of the bridge influence line (IL) ordinate;
I_{N_0} = $N_0 \times N_0$ identity matrix;
I_i = IL ordinate of point i;
I_i^{MAP} = maximum a posteriori IL ordinate of point i;
I_α = inertia moment in numerical model;
I_{Err} = percentage error between maximum a posteriori influence line (MAPIL) and realistic IL;
I_i^{sta} = ith ordinate values of realistic IL;
I_{mid} = midspan position IL ordinate;
$\{I^1\}$ = interval of the IL vector;
$\{\overline{I^1}\}$, $\{\underline{I^1}\}$ = calculated values of the upper and lower bounds of the IL;
K = sampling number of measurements;
$[K_b]$ = vehicle stiffness matrix in numerical model;
k_0 = normalizing constant;
k' = number of samples cutoff;
k_{s1}, k_{s2} = suspension stiffness of the front and the rear axles in numerical model;
k_{t1}, k_{t2} = tire stiffness of the front and rear axles in numerical model;
L = length of the bridge;
L_0 = the transfer matrix representing the input–output relationship of the system;
L_I = identity matrix;
la_i = label value;
M = vehicle weight;
MaxPool = channel-based global maximum pooling;
$[M_b]$ = vehicle mass matrix in numerical model;
$M_c(F)$ = channel attention map output by the channel attention module;
$M_s(F')$ = spatial attention map output by the spatial attention module;
m_1, m_2 = weight of the front and the rear axles in numerical model;
N = number of observations;
N_0 = number of observed degrees of freedom;
N_a = length of the bridge IL vector;
N_d = sum of the number of degrees of freedom;
PF = penalty parameter of the error term defined by the users;
Q = number of vehicles axles;
$\vec{q_i}$ = the vector with label;
$r(e)$ = road roughness at the coordinate of e;
TP = number of positive samples correctly predicted;
Δt = sampling time step;
V = vehicle velocity;
W_i = axle load;
W_i^r = virtual axle load;
$[W^r]$ = virtual axis load matrix;
$[W]_{K,K-C_Q}$ = axle load matrix;
$\underline{w_i}$, $\overline{w_i}$ = lower and upper bounds of weights matrix of the ith axle of a Q-axle vehicle;
$x(t)$ = dynamical system, model response output vector at time t;
$x(0)$ = initial condition of the model;
x_{i0} = central value of the affine form;
x_{i1} = partial deviations;
y_k^T = k-point load effect;
$\{Y\}_{K,1}$ = responses vector collected at each time step;
y_n = measured response;
$\{Y_b\}$ = vehicle displacement vector in numerical model
Y^m = displacement response vector.

α_i, α_j = Lagrange multipliers;
β_h = random phase angle uniformly distributed between 0 and 2π;
$\delta_{nn'}$ = Kronecker delta function;
ε = prediction error;
ε^m = error vector;
ε_i = noise symbols;
θ = unknown parameters;
θ_m = model parameters;
κ = SVM kernel function;
σ = sigmoid function;
ψ = observed data;
ψ_i = value of the ith observation;
$\sum_{\varepsilon}$ = $N_0 \times N_0$ covariance matrix of the prediction error process;
$\phi(q)$ = nonlinear function that maps the input data to the feature space;
Δ_Ω = discrete sampling interval of spatial frequency;
Ω_h = spatial frequency; and
$\otimes$ = element-wise multiplication.

References

Alamdari, M. M., K. Kildashti, B. Samali, and H. V. Goudarzi. 2019. "Damage diagnosis in bridge structures using rotation influence line: Validation on a cable-stayed bridge." *Eng. Struct.* 185: 1–14. https://doi.org/10.1016/j.engstruct.2019.01.124.

Andrieu, C., N. de Freitas, A. Doucet, and M. I. Jordan. 2003. "An introduction to MCMC for machine learning." *Mach. Learn.* 50 (1/2): 5–43. https://doi.org/10.1023/A:1020281327116.

Argyris, C., C. Papadimitriou, P. Panetsos, and P. Tsopelas. 2020. "Bayesian model-updating using features of modal data: Application to the Metsovo Bridge." *J. Sens. Actuator Netw.* 9 (2): 27. https://doi.org/10.3390/jsan9020027.

Au, S.-K. 2011. "Fast Bayesian FFT method for ambient modal identification with separated modes." *J. Eng. Mech.* 137 (3): 214–226. https://doi.org/10.1061/(ASCE)EM.1943-7889.0000213.

Au, S.-K., and Y.-C. Ni. 2014. "Fast Bayesian modal identification of structures using known single-input forced vibration data." *Struct. Control Health Monit.* 21 (3): 381–402. https://doi.org/10.1002/stc.1571.

Beck, J. L. 2010. "Bayesian system identification based on probability logic." *Struct. Control Health Monit.* 17 (7): 825–847. https://doi.org/10.1002/stc.424.

Belegundu, A. D. 1988. "The adjoint method for determining influence lines." *Comput. Struct.* 29 (2): 345–350. https://doi.org/10.1016/0045-7949(88)90269-6.

Bochkovskiy, A., C.-Y. Wang, and H.-Y. M. Liao. 2020. "YOLOv4: Optimal speed and accuracy of object detection." *arXiv arXiv: 2004.10934*. https://doi.org/10.48550/arXiv.2004.10934.

Brigham, E. O. 1988. *The fast Fourier transform and its applications*. Englewood Cliffs, NJ: Prentice-Hall. ser. Signal Processing Series.

Chen, W. Y., H. F. Wang, H. Li, Q. J. Li, Y. Yang, and K. Yang. 2022. "Real-time garbage object detection with data augmentation and feature fusion using SUAV low-altitude remote sensing images." *IEEE Geosci. Remote Sens. Lett.* 19: 6003005. https://doi.org/10.1109/LGRS.2021.3074415.

Chen, Z. C., H. Li, Y. Q. Bao, N. Li, and Y. Jin. 2016. "Identification of spatio-temporal distribution of vehicle loads on long-span bridges using computer vision technology." *Struct. Control Health Monit.* 23 (3): 517–534. https://doi.org/10.1002/stc.1780.

Chen, Z. W., W. B. Yang, J. Li, T. H. Yi, J. C. Wu, and D. D. Wang. 2019. "Bridge influence line identification based on adaptive B-spline basis dictionary and sparse regularization." *Struct. Control Health Monit.* 26 (6): e2355. https://doi.org/10.1002/stc.2355.

Chen, Z.-W., S. Y. Zhu, Y.-L. Xu, Q. Li, and Q.-L. Cai. 2015. "Damage detection in long suspension bridges using stress influence lines." *J. Bridge Eng.* 20 (3): 05014013. https://doi.org/10.1061/(ASCE)BE.1943-5592.0000681.

Cheng, Y. Y., F. Z. Lin, W. G. Wang, and J. Zhang. 2022. "Vision-based trajectory monitoring for assembly alignment of precast concrete bridge components." *Automat. Constr.* 140: 104350. https://doi.org/10.1016/j.autcon.2022.104350.

Cho, S., J. Lee, and S.-H. Sim. 2018. "Comparative study on displacement measurement sensors for high-speed railroad bridge." *Smart Struct. Syst.* 21 (5): 637–652. https://doi.org/10.12989/sss.2018.21.5.637.

Dan, D. H., L. F. Ge, and X. F. Yan. 2019. "Identification of moving loads based on the information fusion of weigh-in-motion system and multiple camera machine vision." *Measurement.* 144: 155–166. https://doi.org/10.1016/j.measurement.2019.05.042.

Dan, D. H., X. W. Yu, F. Han, and B. Xu. 2022. "Research on dynamic behavior and traffic management decision-making of suspension bridge after vortex-induced vibration event." *Struct. Health Monit.* 21 (3): 872–886. https://doi.org/10.1177/14759217211011582.

Degrauwe, D., G. Lombaert, and G. De Roeck. 2010. "Improving interval analysis in finite element calculations by means of affine arithmetic." *Comput. Struct.* 88 (3–4): 247–254. https://doi.org/10.1016/j.compstruc.2009.11.003.

Deng, L., and C. S. Cai. 2010. "Identification of dynamic vehicular axle loads: Theory and simulations." *J. Vib. Control.* 16 (14): 2167–2194. https://doi.org/10.1177/1077546309351221.

Deng, L., L.-L. Duan, W. He, and W. Ji. 2018. "Study on vehicle model for vehicle–bridge coupling vibration of highway bridge in China." *China J. Highway Transport.* 31 (7): 92–100.

Dong, C.-Z., S. Bas, and F. N. Catbas. 2019. "A completely non-contact recognition system for bridge unit influence line using portable cameras and computer vision." *Smart Struct. Syst.* 24 (5): 617–630. https://doi.org/10.12989/sss.2019.24.5.617.

Fang, C., Y.-L. Xu, R. P. Hu, and Z. F. Huang. 2022. "A web-based and design-oriented structural health evaluation system for long-span bridges with structural health monitoring system." *Struct. Control Health Monit.* 29 (2): e2879. https://doi.org/10.1002/stc.2879.

Frøseth, G. T., A. Rønnquist, D. Cantero, and O. Øiseth. 2017. "Influence line extraction by deconvolution in the frequency domain." *Comput. Struct.* 189: 21–30. https://doi.org/10.1016/j.compstruc.2017.04.014.

Fu, H. X., G. Q. Song, and Y. C. Wang. 2021. "Improved YOLOv4 marine target detection combined with CBAM." *Symmetry* 13 (4): 623. https://doi.org/10.3390/sym13040623.

Gelman, A. 2006. "Prior distributions for variance parameters in hierarchical models (comment on article by Browne and Draper)." *Bayesian Anal.* 1 (3): 515–534. https://doi.org/10.1214/06-BA117A.

Han, Y. T., G. Wu, and D. M. Feng. 2022. "Vision-based displacement measurement using an unmanned aerial vehicle." *Struct. Control Health Monit.* 29 (10): e3025. https://doi.org/10.1002/stc.3025.

He, W., L. Deng, H. Shi, C. S. Cai, and Y. Yu. 2017. "Novel virtual simply supported beam method for detecting the speed and axles of moving vehicles on bridges." *J. Bridge Eng.* 22 (4): 04016141. https://doi.org/10.1061/(ASCE)BE.1943-5592.0001019.

Hoffman, M. D., and A. Gelman. 2014. "The no-U-turn sampler: Adaptively setting path lengths in Hamiltonian Monte Carlo." *J. Mach. Learn. Res.* 15: 1593–1623. https://doi.org/10.48550/arXiv.1111.4246.

Hou, J. H., H. Q. Zeng, L. Cai, J. Q. Zhu, J. Chen, and K.-K. Ma. 2019. "Multi-label learning with multi-label smoothing regularization for vehicle re-identification." *Neurocomputing* 345: 15–22. https://doi.org/10.1016/j.neucom.2018.11.088.

Ieng, S.-S. 2015. "Bridge influence line estimation for bridge weigh-in-motion system." *J. Comput. Civ. Eng.* 29 (1): 06014006. https://doi.org/10.1061/(ASCE)CP.1943-5487.0000384.

ISO (International Organization for Standardization). 2016. Mechanical vibration-road surface profiles reporting of measured data. ISO 8605. Geneva, Switzerland: ISO.

Kaipio, J., and E. Somersalo. 2006. *Statistical and computational inverse problems*. New York: Springer Science & Business Media.

Khuc, T., and F. N. Catbas. 2018. "Structural identification using computer vision-based bridge health monitoring." *J. Struct. Eng.* 144 (2): 04017202. https://doi.org/10.1061/(ASCE)ST.1943-541X.0001925.

Klein, N., and T. Kneib. 2016. "Scale-dependent priors for variance parameters in structured additive distributional regression." *Bayesian Anal.* 11 (4): 1071–1106. https://doi.org/10.1214/15-BA983.

Kromanis, R., and P. Kripakaran. 2017. "Data-driven approaches for measurement interpretation: Analysing integrated thermal and vehicular response in bridge structural health monitoring." *Adv. Eng. Inform.* 34: 46–59. https://doi.org/10.1016/j.aei.2017.09.002.

Liao, J. B., G. W. Tang, L. B. Meng, H. G. Liu, and Y. J. Zhang. 2012. "Finite element model updating based on field quasi-static generalized influence line and its bridge engineering application." *Procedia Eng.* 31: 348–353. https://doi.org/10.1016/j.proeng.2012.01.1035.

Liu, Y. S., X. Q. Wang, and F. X. Zhou. 2012. "Study on damage identification of the simply supported beam employ the difference of deflection influence line under symmetrically load." *Appl. Mech. Mater.* 166–169: 1254–1257. https://doi.org/10.4028/www.scientific.net/AMM.166-169.1254.

Liu, Z. W., S. Q. Li, L. H. Wang, B. F. Yan, R. L. Zhang, and Z. Q. Chen. 2022. "Experimental investigation on high-mode vortex-induced vibration of a flexible stay cable in smooth flow." *J. Bridge Eng.* 27 (8): 04022068. https://doi.org/10.1061/(ASCE)BE.1943-5592.0001909.

Mahjoubi, S., R. Barhemat, and Y. Bao. 2020. "Optimal placement of triaxial accelerometers using hypotrochoid spiral optimization algorithm for automated monitoring of high-rise buildings." *Autom. Constr.* 118: 103273. https://doi.org/10.1016/j.autcon.2020.103273.

Moon, J. K., and S. I. Choi. 2000. "Performance of channel estimation methods for OFDM systems in a multipath fading channels." *IEEE T. Consum. Electr.* 46 (1): 161–170. https://doi.org/10.1109/30.826394.

Moore, R. E., R. B. Kearfoot, and M. J. Cloud. 2009. *Introduction to interval analysis*. Philadelphia, PA: Society for Industrial and Applied Mathematics.

Moses, F. 1979. "Weigh-in-motion system using instrumented bridges." *J. Transp. Eng.* 105 (3): 233–249. https://doi.org/10.1061/TPEJAN.0000783.

Neal, R. M. 1992. "An improved acceptance procedure for the hybrid Monte Carlo algorithm." *arXiv*. https://doi.org/10.48550/arXiv.hep-lat/9208011.

Neal, R. M. 1998. "Suppressing random walks in Markov chain Monte Carlo using ordered overrelaxation." *Learn. Graph. Models* 89: 205–228. https://doi.org/10.1007/978-94-011-5014-9_8.

OBrien, E. J., D. Cantero, B. Enright, and A. González. 2010. "Characteristic dynamic increment for extreme traffic loading events on short and medium span highway bridges." *Eng. Struct.* 32 (12): 3827–3835. https://doi.org/10.1016/j.engstruct.2010.08.018.

OBrien, E. J., and B. Enright. 2013. "Using weigh-in-motion data to determine aggressiveness of traffic for bridge loading." *J. Bridge Eng.* 18 (3): 232–239. https://doi.org/10.1061/(ASCE)BE.1943-5592.0000368.

OBrien, E. J., M. J. Quilligan, and R. Karoumi. 2006. "Calculating an influence line from direct measurements." *Proc. ICE-Bridge Eng.* 159: 31–34. https://doi.org/10.1680/bren.2006.159.1.31.

OBrien, E. J., L. W. Zhang, H. Zhao, and D. Hajializadeh. 2018. "Probabilistic bridge weigh-in-motion." *Can. J. Civ. Eng.* 45 (8): 667–675. https://doi.org/10.1139/cjce-2017-0508.

Ojio, T., C. H. Carey, E. J. Obrien, C. Doherty, and S. E. Taylor. 2016. "Contactless bridge weigh-in-motion." *J. Bridge Eng.* 21 (7): 04016032. https://doi.org/10.1061/(ASCE)BE.1943-5592.0000776.

Ojo, O. B., S. Lougue, and W. A. Woldegerima. 2017. "Bayesian generalized linear mixed modeling of Tuberculosis using informative priors." *PLoS One* 12 (3): e0172580. https://doi.org/10.1371/journal.pone.0172580.

Pan, B., K. Li, and W. Tong. 2013. "Fast, Robust and accurate digital image correlation calculation without redundant computations." *Exp. Mech.* 53: 1277–1289. https://doi.org/10.1007/s11340-013-9717-6.

Reddy, B. S., and B. N. Chatterji. 1996. "An FFT-based technique for translation, rotation, and scale-invariant image registration." *IEEE T. Image Process.* 5 (8): 1266–1271. https://doi.org/10.1109/83.506761.

Ren, W.-X., S.-E. Fang, and M.-Y. Deng. 2011. "Response surface–based finite-element-model updating using structural static responses." *J. Eng. Mech.* 137 (4): 248–257. https://doi.org/10.1061/(ASCE)EM.1943-7889.0000223.

Rowley, C. W., E. J. Obrien, A. Gonzalez, and A. Žnidarič. 2009. "Experimental testing of a moving force identification bridge weigh-in-motion algorithm." *Exp. Mech.* 49: 743–746. https://doi.org/10.1007/s11340-008-9188-3.

Siwowski, T., M. Rajchel, T. Howiacki, R. Sieńko, and Ł Bednarski. 2021. "Distributed fibre optic sensors in FRP composite bridge monitoring: Validation through proof load tests." *Eng. Struct.* 246: 113057. https://doi.org/10.1016/j.engstruct.2021.113057.

Smola, A. J., and B. Schölkopf. 2004. "A tutorial on support vector regression." *Stat. Comput.* 14 (3): 199–222. https://doi.org/10.1023/B:STCO.0000035301.49549.88.

Sousa, H., F. Cavadas, A. Henriques, J. Bento, and J. Figueiras. 2013. "Bridge deflection evaluation using strain and rotation measurements." *Smart Struct. Syst.* 11 (4): 365–386. https://doi.org/10.12989/sss.2013.11.4.365.

Stolfi, J., and L. H. De Figueiredo. 1997. "Self-validated numerical methods and applications." In *Monograph for 21st Brazilian Mathematics Colloquium*, edited by J. Stolfi and L. Henrique de Figueiredo, 15–86. Rio de Janeiro: Citeseer.

Strauss, A., R. Wendner, D. M. Frangopol, and K. Bergmeister. 2012. "Influence line-model correction approach for the assessment of engineering structures using novel monitoring techniques." *Smart Struct. Syst.* 9 (1): 1–20. https://doi.org/10.12989/sss.2012.9.1.001.

Sun, H., D. M. Feng, Y. Liu, and M. Q. Feng. 2015. "Statistical regularization for identification of structural parameters and external loadings using state space models." *Comput. Aided Civ. Infrastruct.* 30 (11): 843–858. https://doi.org/10.1111/mice.12169.

Tang, X. Y., H. S. Song, W. Wang, and Y. N. Yang. 2020. "Vehicle spatial distribution and 3D trajectory extraction algorithm in a cross-camera traffic scene." *Sensors* 20 (22): 6517. https://doi.org/10.3390/s20226517.

Wang, N.-B., L.-X. He, W.-X. Ren, and T.-L. Huang. 2017. "Extraction of influence line through a fitting method from bridge dynamic response induced by a passing vehicle." *Eng. Struct.* 151: 648–664. https://doi.org/10.1016/j.engstruct.2017.06.067.

Wang, R., Z. Y. Wang, Z. W. Xu, C. Wang, Q. Li, Y. X. Zhang, and H. Li. 2021. "A real-time object detector for autonomous vehicles based on YOLOv4." *Comput. Intel. Neurosc.* 2021: 9218137. https://doi.org/10.1155/2021/9218137.

Wesner, J. S., and J. P. F. Pomeranz. 2021. "Choosing priors in Bayesian ecological models by simulating from the prior predictive distribution." *Ecosphere* 12 (9): e03739. https://doi.org/10.1002/ecs2.3739.

Woo, S., J. Park, J.-Y. Lee, and I. S. Kweon. 2018. "CBAM: Convolutional block attention module." In Vol. 11211 of *Proc., European Conf. on Computer Vision (ECCV)*, 3–19. Cham, Switzerland: Springer.

Wu, B. T., G. Wu, H. X. Lu, and D.-C. Feng. 2017. "Stiffness monitoring and damage assessment of bridges under moving vehicular loads using spatially-distributed optical fiber sensors." *Smart Mater. Struct.* 26 (3): 035058. https://doi.org/10.1088/1361-665X/aa5c6f.

Wu, Z. Y., K. Zhou, H. W. Shenton, and M. J. Chajes. 2019. "Development of sensor placement optimization tool and application to large-span cable-stayed bridge." *J. Civil Struct. Health Monit.* 9: 77–90. https://doi.org/10.1007/s13349-018-0320-5.

Xia, Y., X. D. Jian, B. Yan, and D. Su. 2019. "Infrastructure safety oriented traffic load monitoring using multi-sensor and single camera for short and medium span bridges." *Remote Sens.* 11 (22): 2651. https://doi.org/10.3390/rs11222651.

Xiao, X., Y. L. Xu, and Q. Zhu. 2015. "Multiscale modeling and model updating of a cable-stayed bridge. II: Model updating using modal frequencies and influence lines." *J. Bridge Eng.* 20 (10): 04014113. https://doi.org/10.1061/(ASCE)BE.1943-5592.0000723.

Yan, B. F., D. R. Li, W. B. Chen, L. Deng, and X. M. Jiang. 2021. "Mode shape–aided cable force determination using digital image correlation." *Struct. Health Monit.* 20 (5): 2430–2445. https://doi.org/10.1177/1475921720952163.

Yan, W.-J., and K.-V. Yuen. 2020. "A new probabilistic frequency-domain approach for influence line extraction from static transmissibility measurements under unknown moving loads." *Eng. Struct.* 216: 110625. https://doi.org/10.1016/j.engstruct.2020.110625.

Yang, D.-H., Z.-X. Guan, T.-H. Yi, H.-N. Li, and Y.-S. Ni. 2022. "Fatigue evaluation of bridges based on strain influence line loaded by elaborate stochastic traffic flow." *J. Bridge Eng.* 27 (9): 04022082. https://doi.org/10.1061/(ASCE)BE.1943-5592.0001929.

Yao, X.-J., T.-H. Yi, C. X. Qu, and H.-N. Li. 2018. "Blind modal identification using limited sensors through modified sparse component analysis by time-frequency method." *Comput. Aided Civ. Infrastruct.* 33 (9): 769–782. https://doi.org/10.1111/mice.12372.

Yuen, K.-V. 2010. *Bayesian methods for structural dynamics and civil engineering*. Singapore: Wiley.

Yuen, K.-V., and L. S. Katafygiotis. 2003. "Bayesian fast Fourier transform approach for modal updating using ambient data." *Adv. Struct. Eng.* 6 (2): 81–95. https://doi.org/10.1260/136943303769013183.

Zaurin, R., and F. N. Catbas. 2010a. "Structural health monitoring using video stream, influence lines, and statistical analysis." *Struct. Health Monit.* 10 (3): 309–332. https://doi.org/10.1177/1475921710373290.

Zaurin, R., and F. N. Catbas. 2010b. "Integration of computer imaging and sensor data for structural health monitoring of bridges." *Smart Mater. Struct.* 19 (1): 015019. https://doi.org/10.1088/0964-1726/19/1/015019.

Zeinali, Y., and B. A. Story. 2018. "Impairment localization and quantification using noisy static deformation influence lines and Iterative Multi-parameter Tikhonov Regularization." *Mech. Syst. Signal Process.* 109: 399–419. https://doi.org/10.1016/j.ymssp.2018.02.036.

Zhang, B., L. M. Zhou, and J. Zhang. 2019. "A methodology for obtaining spatiotemporal information of the vehicles on bridges based on computer vision." *Comput. Aided Civ. Infrastruct. Eng.* 34 (6): 471–487. https://doi.org/10.1111/mice.12434.

Zhang, F.-L., S.-K. Au, and H.-F. Lam. 2015. "Assessing uncertainty in operational modal analysis incorporating multiple setups using a Bayesian approach." *Struct. Control Health Monit.* 22 (3): 395–416. https://doi.org/10.1002/stc.1679.

Zhang, L., X. X. Cheng, G. Wu, and T. Y. Wang. 2022. "Reference-free damage identification method for highway continuous girder bridges based on long-gauge fibre Bragg grating strain sensors." *Measurement* 195: 111064. https://doi.org/10.1016/j.measurement.2022.111064.

Zhao, H., N. Uddin, X. D. Shao, P. Zhu, and C. J. Tan. 2015. "Field-calibrated influence lines for improved axle weight identification with a bridge weigh-in-motion system." *Struct. Infrastruct. Eng.* 11 (6): 721–743. https://doi.org/10.1080/15732479.2014.904383.

Zheng, X., D.-H. Yang, T.-H. Yi, and H.-N. Li. 2019a. "Development of bridge influence line identification methods based on direct measurement data: A comprehensive review and comparison." *Eng. Struct.* 198: 109539. https://doi.org/10.1016/j.engstruct.2019.109539.

Zheng, X., D.-H. Yang, T.-H. Yi, and H.-N. Li. 2020. "Bridge influence line identification from structural dynamic responses induced by a high-speed vehicle." *Struct. Control Health Monit.* 27 (7): e2544. https://doi.org/10.1002/stc.2544.

Zheng, X., D.-H. Yang, T.-H. Yi, H.-N. Li, and Z.-W. Chen. 2019b. "Bridge influence line identification based on regularized least-squares QR decomposition method." *J. Bridge Eng.* 24 (8): 06019004. https://doi.org/10.1061/(ASCE)BE.1943-5592.0001458.

Zheng, X., T.-H. Yi, J.-W. Zhong, and D.-H. Yang. 2022. "Rapid evaluation of load-carrying capacity of long-span bridges using limited testing vehicles." *J. Bridge Eng.* 27 (4): 04022008. https://doi.org/10.1061/(ASCE)BE.1943-5592.0001838.

Zhou, Y., Y. L. Pei, Z. W. Li, L. Fang, Y. Zhao, and W. J. Yi. 2020. "Vehicle weight identification system for spatiotemporal load distribution on bridges based on non-contact machine vision technology and deep learning algorithms." *Measurement* 159: 107801. https://doi.org/10.1016/j.measurement.2020.107801.

Zhou, Y., Y. L. Pei, S. Zhou, Y. Zhao, J. X. Hu, and W. J. Yi. 2021a. "Novel methodology for identifying the weight of moving vehicles on bridges using structural response pattern extraction and deep learning algorithms." *Measurement* 168: 108384. https://doi.org/10.1016/j.measurement.2020.108384.

Zhou, Y., S. Zhou, L. Deng, and C. B. Chen. 2019. "Research on moving load identification based on measured acceleration and strain signals." *Int. J. Lifecycle Perform. Eng.* 3 (4): 257–288. https://doi.org/10.1504/IJLCPE.2019.103696.

Zhou, Y., S. Zhou, G. W. Hao, and J. Zhang. 2021b. "Bridge influence line identification based on big data and interval analysis with affine arithmetic." *Measurement* 183: 109807. https://doi.org/10.1016/j.measurement.2021.109807.

Zhu, Y. J., H. Sekiya, T. Okatani, I. Yoshida, and S. Hirano. 2022. "Real-time vehicle identification using two-step LSTM method for acceleration-based bridge weigh-in-motion system." *J. Civil Struct. Health Monit.* 12: 689–703. https://doi.org/10.1007/s13349-022-00576-2.